Diagrammatic Approach for Constructing Multiresolution of Primal Subdivisions

Richard Bartels

University of Waterloo

Ali Mahdavi-Amiri, Faramarz Samavati

University of Calgary

Nezam Mahdavi-Amiri

Sharif University of Technology

Abstract

It is possible to define multiresolution by reversing the process of subdivision. One approach to reverse a subdivision scheme appropriates pure numerical algebraic relations for subdivision using the interaction of diagrams [1, 2]. However, certain assumptions carried through the available work, two of which we wish to challenge: (1) the construction of multiresolutions for irregular meshes are reconsidered in the presence of any extraordinary vertex rather than being prepared beforehand as simple available relations and (2) the connectivity graph of the coarse mesh would have to be a subgraph of the connectivity graph of the fine mesh. $\sqrt{3}$ subdivision [3] lets us engage both of these concerns. With respect to (2), the $\sqrt{3}$ post-subdivision connectivity graph shares no interior edge with the pre-subdivision connectivity graph. With respect to (1), we observe that no subdivision produces an arbitrary connectivity graph. Rather, there are local regularities imposed by the subdivision on the fine mesh, which may be exploited to establish, in advance, the decomposition and reconstruction filters of a multiresolution for an initially given irregular coarse mesh. We provide indications that our proposed approach for $\sqrt{3}$ subdivision is potentially useful for other primal subdivision schemes by mentioning results for the Loop [4] and Catmull-Clark subdivisions [5]. Finally, after showing some results, we analyze the quality of the reversal matrix and present a technique using numerical optimization.

Keywords: Subdivision, Least squares, Multiresolution, Biorthogonality

1. Introduction

Multiresolution surfaces have found many applications in computer graphics and scientific visualization. In multiresolution, objects can be efficiently and elegantly represented, and analyzed at multiple levels of detail. In this representation, a high resolution approximation of a surface can be decomposed into a lower resolution approximation and a hierarchical sequence of detail information that together provide a complete reconstruction of the original surface.

There are two main approaches for establishing a multiresolution representation: *functional* and *discrete*. In the functional approach (see e.g., [6, 7]), from a sequence of nested basis functions (refinable scale functions) $\{\phi_n^j\}$, the complementary basis functions $\{\psi_n^j\}$ (or wavelet functions) are determined. The complete sets of $\{\phi_n^j\}$ and $\{\psi_n^j\}$ are used to construct a multiresolution analysis.

In the discrete approach, a multiresolution is constructed using reverse subdivision for a given subdivision scheme. To build a multiresolution by reversing subdivision, two general methods have been proposed: operative and diagrammatic. In the operative approach, reverse subdivision filters are designed based on geometric and topological operations used in the subdivision scheme. Examples of this approach can be found in [8, 9, 10, 11, 12]. The diagrammatic approach contains methods that systematically generate multiresolution filters based on linear equations being constructed to achieve certain conditions from the interaction of multiresolution filters (e.g., biorthogonality conditions). This approach benefits from linear algebra and matrix computations and may take advantage of many numerical techniques. As shown in [13], for curves and tensor-product surfaces, due to their regular structures, it is not hard to build a multiresolution in this way. However, it has not been previously clear how to use the diagrammatic approach for general meshes. Previous attempts in diagrammatic approaches were either limited to regular meshes or suffered from lack of generality, meaning that in the presence of any extraordinary vertex in the diagram, a new set-up had to be made to define the multiresolution matrices.

Here, for the first time, we generalize diagrammatic approaches for subdivisions of a general surface and provide a method to deal with extraordinary vertices. In our proposed method, we represent general rows/columns of multiresolution matrices by diagrams and translate matrix multiplications into interactions between these diagrams. Diagrams can be considered as a generalization of subdivision masks in which the connectivity of contributing vertices and their weights are represented. From interactions of the diagrams, we derive certain linear equations to establish biorthogonality relationships of multiresolution filters. We examine our new method for $\sqrt{3}$ subdivision and mention

2

how to apply it for the Catmull-Clark and Loop subdivision schemes. Matrices that we obtain for these subdivision schemes are consistent with the resulting filters due to multiresolution techniques of the operative approach.

Our method takes advantage of the local effects of extraordinary vertices in subdivision surfaces by observing that these vertices cannot be entirely arbitrary in nature. From a given starting mesh, each subdivision acts on any vertex in a limited possible way, and all meshes refined from the starting mesh have only a limited collection of extraordinary vertices. Using this fact, as we show in $\sqrt{3}$ subdivision, and indicate in the Loop and Catmull-Clark schemes, it may be possible to catalog the multiresolution filters for any vertex in the limited collection. In addition to the construction of these filters, we analyze the quality of the reversal matrix by quantifying the local deviation after decomposition and discuss how to improve this deviation using a least squares model.

Our proposed method here is designed for primal subdivisions in which the set of the vertices before subdivision is a subset of vertices after subdivision. Discussion about finding multiresolution for dual subdivisions such Doo-Sabin is out of scope of our work here; interested readers may consult [12]. We note that similar to other multiresolution methods constructed by reversing the subdivision process [1, 8, 9, 12, 14], the input of our multiresolution method needs to be semiregular (i.e., a mesh with subdivision connectivity). Fortunately, this constraint is not too restrictive as such meshes are rapidly becoming more popular [15, 16] and there exist various remeshing techniques to convert an arbitrary mesh to a semiregular one [17].

2. Related Work

Multiresolution analysis provides a means to transition from a high to a low resolution and vice versa [18]. Several methods have been proposed to reduce the resolution of an object for applications such as mesh morphing, compression, or view dependent rendering [18, 19, 20, 21, 22]. These methods can be constructed using three main categories of functional methods, diagrammatic approaches, and operative approaches. In the following, we describe related work for each of these categories. In addition to these methods, spectral mesh processing also exist that rely on the classical discrete Fourier analysis and mesh Laplacian. However, here, we do not discuss such methods as we do not follow the same approach. An interested reader may refer to [23, 24].

2.1. Functional Methods

One way to define multiresolution is to solely work with basis functions spanning a vector space [6, 25]. In fact, a function that belongs to a linear function space V^k can be represented as a vector $\mathbf{c} = [\mathbf{c_0}, \mathbf{c_1}, ...]$, in which $\mathbf{c_i}$ is the coefficient of the ith basis function of V^k . The basis functions of V^k are also referred to as *scaling functions* and are denoted by ϕ_i^k. The set of all scaling functions for V^k is denoted by $\Phi^k(u) = \left[\phi_0^k, \phi_1^k, ...\right]$.

Subdivision can be defined in terms of scaling functions. Assume that we have a set of points $\mathbf{c}$ and we obtain a new set of points $\mathbf{f}$ using subdivision $\mathbf{P}$; $(\mathbf{f} = \mathbf{Pc})$. If we consider these two sets of points as the coefficients of scaling functions, we would have

$$\Phi^{k-1}(u) \quad = \quad \Phi^k(u)\mathbf{P}. \tag{2.1}$$

An additional space, W^k, called the *wavelet space*, is also needed in multiresolution analysis. W^k is the complementary space of V^k to span V^{k+1}. Basis functions of the wavelet space W^k are usually denoted by $\Psi^k(u) = \left[\psi_0^k, \psi_1^k, ...\right]$. We can also represent Ψ^k in terms of scaling functions as

$$\begin{aligned} \Psi^{k-1}(u) &= \Phi^k(u)\mathbf{Q}, \\ \left[\Phi^{k-1}|\Psi^{k-1}\right] &= \Phi^k \left[\mathbf{P}|\mathbf{Q}\right]. \end{aligned} \tag{2.2}$$

The matrices $\mathbf{P}$ and $\mathbf{Q}$ are used to perform a reconstruction (i.e., transition from resolution $k-1$ to resolution k). However, decomposition, which is a transition from resolution k to resolution $k-1$, is also necessary. As a result, Φ^k is decomposed into its complementary basis functions Φ^{k-1} and $\Psi^k - 1$ by

$$\left[\Phi^{k-1}|\Psi^{k-1}\right] \left[\frac{\mathbf{A}}{\mathbf{B}}\right] \quad = \quad \Phi^k.$$

Having equations (2.2) and (2.3), we come up with the following relations between multiresolution matrices:

$$\left[\frac{\mathbf{A}}{\mathbf{B}}\right] \quad = \quad [\mathbf{P}|\mathbf{Q}]^{-1} \Longrightarrow$$

$$\left[\begin{array}{c} \mathbf{A} \\ \hline \mathbf{B} \end{array}\right] [\mathbf{P}|\mathbf{Q}] \quad = \quad \left[\begin{array}{cc} \mathbf{I} & 0 \\ 0 & \mathbf{I} \end{array}\right]. \tag{2.3}$$

Constructing multiresolutions using the functional approach has been extensively studied in the literature. There are mainly three categories of multiresolution in this setting, involving wavelets that are *orthogonal*, *semi-orthogonal*, and *biorthogonal*. In orthogonal wavelets, the scaling functions are orthogonal to one another and every wavelet is orthogonal to every coarser scaling function. In addition, the wavelets are orthogonal to one another [18]. Semi-orthogonal wavelets relax the orthogonality conditions by only requiring that each wavelet is orthogonal to all coarser scaling functions [26]. Biorthogonal wavelets, however, are merely required to satisfy one condition, namely, to have $[\mathbf{P}|\mathbf{Q}]$ invertible. Note that $\mathbf{c}$ is a set of coarse vertices and $\mathbf{f}$ is the set of subdivided vertices with $\mathbf{f} = \mathbf{Pc}$. If $\mathbf{f}$ is perturbed by some vectors, $\mathbf{g} = \mathbf{f} + \mathbf{e}$ is obtained. The set of coarse vertices and detail vectors are found as linear combinations of vertices in $\mathbf{g}$, shown in a matrix notation by $\bar{\mathbf{c}} = \mathbf{Ag}$ and $\mathbf{d} = \mathbf{Bg}$. Having $\bar{\mathbf{c}}$ and $\mathbf{d}$, the perturbed vertices $\mathbf{g}$ can be reconstructed as $\mathbf{g} = \mathbf{P}\bar{\mathbf{c}} + \mathbf{Qd}$. One approach to construct biorthogonal wavelets is the lifting process, in which matrices $\mathbf{P}$, $\mathbf{Q}$, $\mathbf{A}$, and $\mathbf{B}$ are initially constructed. Then, a lifting matrix L modifies the original scheme as $\mathbf{Q_{lift}} = \mathbf{A} + L\mathbf{B}$ and $\mathbf{A_{lift}} = \mathbf{Q} - \mathbf{P}L$ [27]; matrices $\mathbf{P}$ and $\mathbf{B}$ remain unchanged.

2.2. Diagrammatic Approach

With the motivation of extending matrix representations to non tensor product surfaces, Samavati and Bartels [2] defined diagrammatic tools that are regular patterns of value-labeled nodes. To determine the multiresolution filters for the regular setting, they extended matrix-matrix interactions to diagram-diagram interactions. From these interactions, a method of multiresolution construction was introduced where two systems of linear equations and a bilinear system of equations were formed. Multiresolution filters were found from the solutions of these systems. In [1], using diagram interactions, a new construction was introduced which did not require any bilinear equations. In this work, using SVD, Bartels and Samavati defined diagrammatic tools for meshes with regular vertices. However, multiresolution for a general connectivity mesh using the diagrammatic approach has not been established before. Here, we show how to establish such a general construction by examining the $\sqrt{3}$, and sketching the Loop and Catmull-Clark subdivision schemes.

5

2.3. Operative Approach

In contrast to diagrammatic approaches in which all the relations are introduced using linear systems resulting from diagram interactions, in an operative approach, multiresolution filters are directly constructed from the specific definition and properties of a given subdivision mask. In the operative approach, reverse subdivision filters are produced by isolating a coarse point and defining its positions based on its neighborhood. In order to reconstruct without losing any information, additional detail vectors are needed. Having possibly more than one solution for coarse points and details, constraints can be imposed to limit the space of possible solutions.

In the constrained wavelet approach [8], a constraint is that the details for old vertices are defined as a linear combination of details of new vertices. After finding coarse approximations and details, similar to lifting schemes, coarse approximations are improved. To do so, an additional smoothing step is performed on the constraining wavelets to reduce the local deviations and improve upon the reverse subdivision. As a result, in the constrained wavelet approach, reverse subdivision filters can be divided into two parts, one of finding a coarse approximation and the other of smoothing. In this process, initially details and coarse approximations are determined. Afterwards, coarse approximations are smoothed to get better approximations using an optimization scheme that provides a smoothing vector. In [8, 9], the Loop and Catmull-Clark filters are obtained using constraining wavelets. Mahdavi-Amiri and Samavati have used the same approach to find the $\sqrt{3}$ and $\sqrt{2}$ reverse subdivision filters [10, 11]. In 10, we discuss how one can use a similar approach to reduce the local deviations of our proposed multiresolution.

2.3.1. Smooth Reverse Subdivision

We pointed out that a smoothing vector is used to reduce the magnifying effect of reverse subdivision. However, the resulting meshes of reverse subdivision can be still very coarse. As a result, smooth reverse subdivision is proposed to improve upon the results. The basic idea of smooth reverse subdivision [28] is to perturb coarse approximations by a vector to minimize an energy function $E_{total}(\Delta) = \omega E_{sub}(\Delta) + (1-\omega)E_{smooth}(\Delta)$ in which E_{sub} is the Euclidean distance between fine points and subdivided coarse approximations and E_{smooth} is the energy of a coarse approximation vertex in its local neighborhood. Perturbation vectors for the Catmull-Clark and Loop subdivisions are proposed in [29]. Using this method, Mahdavi-Amiri and Samavati [10, 11] provided filters for smooth $\sqrt{3}$ and $\sqrt{2}$ reverse subdivision methods.

6

The approach presented in [1, 2, 13, 30] follows the outline for development of biorthogonal multiresolutions that can be found in the literature; e.g., see [31]. As in much of the wavelet literature, the main attention in these publications was on multiresolutions in regular settings. In [1], numerical constructions were offered for irregular settings, but they inadequately required computations on the fly for any extraordinary vertex rather than using predetermined formulas. Here, we intend to overcome this inadequacy.

3. Overview of Our Work

The construction assumes only that a *subdivision* is defined, which may be expressed using a *subdivision matrix* $\mathbf{P}$, applied to a *coarse mesh* of points $\mathbf{c}$ to produce a *fine mesh* of points $\mathbf{f}$:

$$\mathbf{f} = \mathbf{P}\mathbf{c}. \tag{3.1}$$

The matrices $\mathbf{P}$ for subdivisions are sparse and patterned. Specifically, each of the $|\mathbf{f}|$ fine points is produced *locally* as an affine combination of the $|\mathbf{c}|$ coarse points lying in a small geometric neighborhood. The coefficients in the combination constitute the entries in a row of $\mathbf{P}$ that yields the fine point. In primal subdivisions, the fine points fall into two categories: either $(|\mathbf{f}| - |\mathbf{c}|)$ *newly created points* or $|\mathbf{c}|$ pre-existing points whose *positions have been adjusted*. Figure 1 shows this schematically, with the squares in the bottom diagram indicating the created points and the circles representing the adjusted points. There, c_0 and c_3, for example, have moved to adjusted positions f_0 and f_6, while f_1 and f_3 are new.

Figure 2 augments Figure 1 emphasizing the local nature of the action of $\mathbf{P}$ on $\mathbf{c}$ by showing the contribution a coarse point makes to each fine point that it influences. For example, for each coarse point c_κ there is one associated column, $\mathbf{p}_\kappa$ of $\mathbf{P}$, and $\mathbf{f} = \cdots + \mathbf{p}_\kappa c_\kappa + \cdots$. In particular, the fine point $f_k = \sum_\kappa p_{k,\kappa} c_\kappa$, where $p_{k,\kappa}$ is the kth component of column $\mathbf{p}_\kappa$. If we transcribe each nonzero $p_{k,\kappa}$ onto its f_k node, we can easily see how many, and which, fine points are influenced by c_κ. In Figure 2, at the top we see the influence of c_0 and in the middle we see the influence of c_3. These are $\mathbf{P}$ *column diagrams* associated with c_0 and c_3 respectively.

For construction in [1, 13] first finds a *reversal matrix*, $\mathbf{A}$, that satisfies $\mathbf{A}\mathbf{P} = \mathbf{I}$, and consequently,

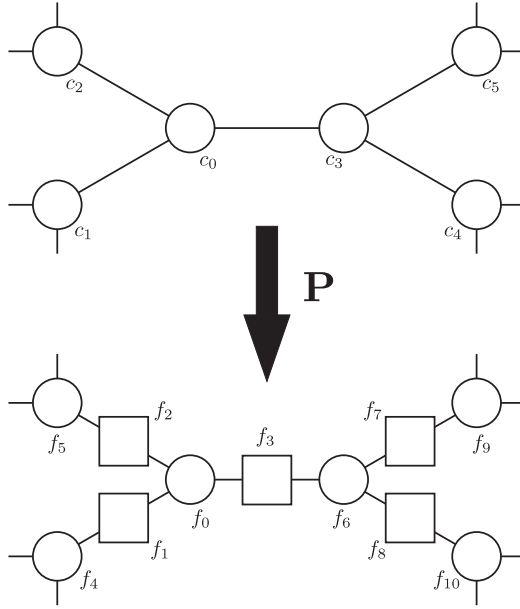$$\mathbf{c} = \mathbf{A}\mathbf{f}. \tag{3.2}$$

7

Figure 1: Coarse to fine subdivision.

The construction of the reversal, *local least squares fitting* is needed to find $\mathbf{A}$, one row at a time. The κth row $\mathbf{a}_\kappa$ of $\mathbf{A}$ provides an approximation of the position of the coarse point c_κ whose displaced-point image in the fine mesh is f_k. To construct $\mathbf{a}_\kappa$, a geometric neighborhood of fine points is taken that includes the fine points around f_k whose positions are defined by affine combinations involving c_κ. Figure 2 at the bottom shows an $\mathbf{A}$ *row diagram* for recovering the position of c_0 from its subdivision image f_0 together with all the nearby fine points influenced by c_0. The position would be given as $c_0 = \sum_{j=0}^{6} a_{0,j} f_j$. For c_0 to be a least squares fit of $f_0, \ldots, f_6$ with respect to an associated submatrix of $\mathbf{P}$, the components of $\mathbf{a}_0$ are determined to meet the following conditions: (1) the row-column product $\mathbf{a}_0 \mathbf{p}_0$ must equal 1; (2) all row-column products of $\mathbf{a}_0$ with the other columns of $\mathbf{P}$ must be zero; (3) the vector $\mathbf{a}_0$ must have the least Euclidean norm among all solutions. This last condition, on the minimality of the norm of $\mathbf{a}_0$, is what makes $\mathbf{a}_0$ a local least squares solution. The discussion for establishing this constitutes Section 3.3 of [13].
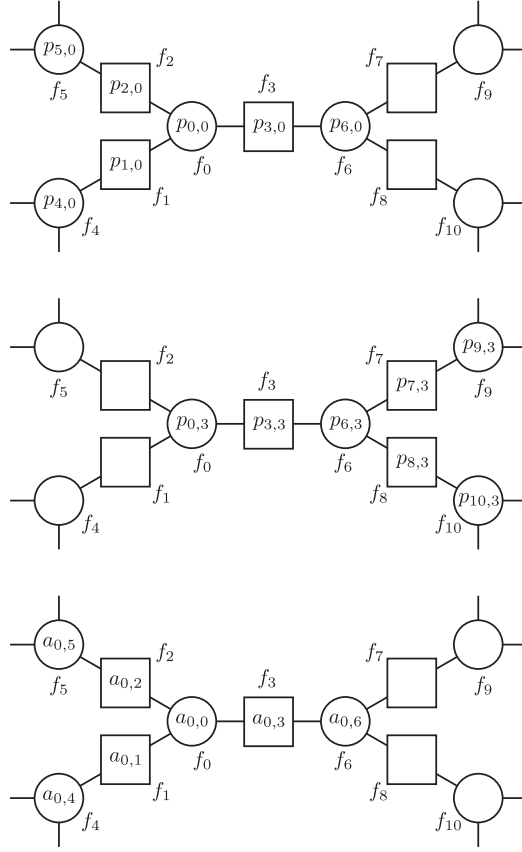
8

Figure 2: $\mathbf{P}$ diagrams for $c_0 \to f_0$ and $c_3 \to f_6$ and $\mathbf{A}$ diagram for $f_0 \to c_0$.

So, looking at the example of Figure 2,

$$a_{0,0}p_{0,0} + a_{0,1}p_{1,0} + a_{0,2}p_{2,0} + a_{0,3}p_{3,0} + a_{0,4}p_{4,0} + a_{0,5}p_{5,0} = 1$$
$$\sum_j a_{0,j}p_{j,\ell} = 0, \ \ell \neq 0 \tag{3.3}$$
$$\sum_j a_{0,j}^2 = \min.$$

Included in the second line of (3.3), for $\ell = 3$, is the interaction of the diagram of $\mathbf{a}_0$ at the bottom of Figure 2 with the middle diagram of that figure, namely, for illustration:

$$a_{0,0}p_{0,3} + a_{0,3}p_{3,3} + a_{0,6}p_{6,3} = 0.$$

Suppose a mesh of fine points $\mathbf{g}$ has subdivision connectivity consistent with $\mathbf{P}$, but, $\mathbf{g} \neq \mathbf{Pc}$ for all $\mathbf{c}$. Such situations arise when the points of $\mathbf{g}$ are measured from a physical object, or when the fine points $\mathbf{f} = \mathbf{Pc}$, for some $\mathbf{c}$, are displaced into positions $\mathbf{g}$ by editing in an interactive manner.

9

We may produce coarse points $\bar{\mathbf{c}} = \mathbf{A}\mathbf{g}$, but if we apply $\mathbf{P}$ to $\bar{\mathbf{c}}$, we will only produce $\mathbf{g}$ plus some error $\mathbf{e}$ as follows:

$$\mathbf{g} = \mathbf{P}\bar{\mathbf{c}} + \mathbf{e}. \tag{3.4}$$

To correct for the error $\mathbf{e}$, the construction finds two more matrices, the *detail matrix* $\mathbf{B}$ and the *correction matrix* $\mathbf{Q}$, such that

$$\mathbf{d} = \mathbf{B}\mathbf{g}, \tag{3.5}$$

and

$$\mathbf{e} = \mathbf{Q}\mathbf{d}. \tag{3.6}$$

The rows of the matrices $\mathbf{A}$ and $\mathbf{B}$ provide *decomposition filters* that may be applied to a fine mesh $\mathbf{g}$ to obtain, respectively, a *coarse approximation* $\bar{\mathbf{c}}$ to $\mathbf{g}$ and *detail information* $\mathbf{d}$ for $\mathbf{g}$. The rows of the matrices $\mathbf{P}$ and $\mathbf{Q}$ provide *reconstruction filters* that yield $\mathbf{g}$ as

$$\mathbf{g} = \mathbf{P}\bar{\mathbf{c}} + \mathbf{Q}\mathbf{d}. \tag{3.7}$$

The matrix $\mathbf{Q}$ is generated from $\mathbf{A}$ one column at a time. Each column of $\mathbf{Q}$ starts with a geometric neighborhood which determines a submatrix of $\mathbf{A}$, and the submatrix, in turn, defines a null space of $\mathbf{A}$ in which the column of $\mathbf{Q}$ is required to lie. The $\mathbf{Q}$ resulting from determining all columns in this way is sparse and patterned.

The matrix $\mathbf{B}$ is generated in two steps [1]. A matrix $\mathbf{T}$ is constructed from $\mathbf{Q}$, row by row, as a left inverse, that is, $\mathbf{T}\mathbf{Q} = \mathbf{I}$, in the same manner as $\mathbf{A}$ was constructed from $\mathbf{P}$. Then, $\mathbf{B} = \mathbf{T}(\mathbf{I} - \mathbf{P}\mathbf{A})$. The resulting $\mathbf{B}$ is sparse and patterned.

Each column of $\mathbf{Q}$ can be represented by a column diagram referenced to one of the newly created points of $\mathbf{f}$, and likewise for each row of $\mathbf{B}$. $\mathbf{Q}$, $\mathbf{T}$ and $\mathbf{B}$ are constructed with the aid of row and column diagrams in much the same way as $\mathbf{A}$.

In our work here we initially carry out the construction for the $\sqrt{3}$ subdivision [3]. This contribution is discussed in details. Later, we briefly show how to derive the Loop and Catmull-Clark multiresolution masks using the same construction. The $\mathbf{P}$ column diagrams are presented in Section 4. The construction of $\mathbf{A}$ row diagrams follows in Section 5. The presentation ends with the construction of the $\mathbf{Q}$ column diagrams and the $\mathbf{B}$ row diagrams respectively in Section 6 and Section 7. In Section 8, we discuss the possibility of using this method for other subdivision schemes such as Loop and Catmull-Clark. Handling the boundary of $\sqrt{3}$ subdivision and its reverse is also discussed in Section 9.

10

We chose to investigate $\sqrt{3}$ subdivision since the mesh-to-mesh behavior of the subdivision is novel for the local least squares construction. In all previous studies that generated multiresolutions using this construction, the edges of the coarse mesh were repeated (usually with extra nodes along their length) in the fine mesh. The coarse mesh was, in a sense, a submesh of the fine mesh. This is not the case in a single step of $\sqrt{3}$ subdivision. We later describe how we can apply this construction on the more straightforward Loop and Catmull-Clark subdivisions.
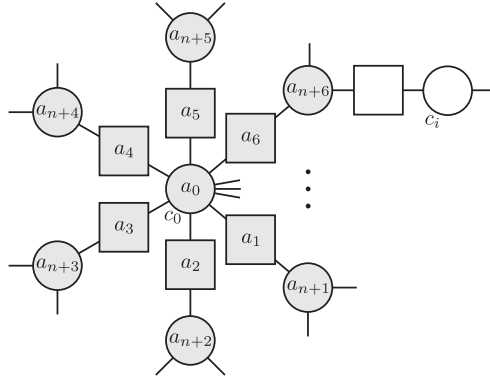
Figure 3: A point with valence n.

A new result of our work here is the capability to handle *extraordinary points* in a diagrammatic approach. Such a point in a mesh is one that has a valence different from that of a regular point (valence six for triangular meshes and valence four for quadrilateral meshes). It is a feature of primal subdivisions that, after one or more steps of applying $\mathbf{P}$, extraordinary points find themselves isolated in a neighborhood of regular points, as shown in Figure 3. This observation opens the way to constructing $\mathbf{A}$, and subsequently $\mathbf{Q}$ and $\mathbf{B}$, in a more general way. We extend diagrams for extraordinary points and construct multiresolution masks for $\sqrt{3}$, Loop and Catmull-Clark subdivisions.

Figure 3 mainly presents an overview of the issues in constructing $\mathbf{A}$. It indicates the $\mathbf{P}$ column diagram associated with c_0, where the nodes of the diagram are shaded. Indeed, c_0 is the *central node* of the diagram with valence n. The nodes to be occupied by the resulting $\mathbf{A}$ row diagram in order to recover the position of c_0 from the points of the fine mesh are labeled. We show that as the valence n is increased, a nested system of equations (3.3) is generated with solutions a_j as functions of n. Such a nested system for $\sqrt{3}$ subdivision is indicated by (5.1) of Section 5.

The local least squares $\mathbf{A}$ filters of width two for $\sqrt{3}$, Loop and Catmull-Clark subdivisions all
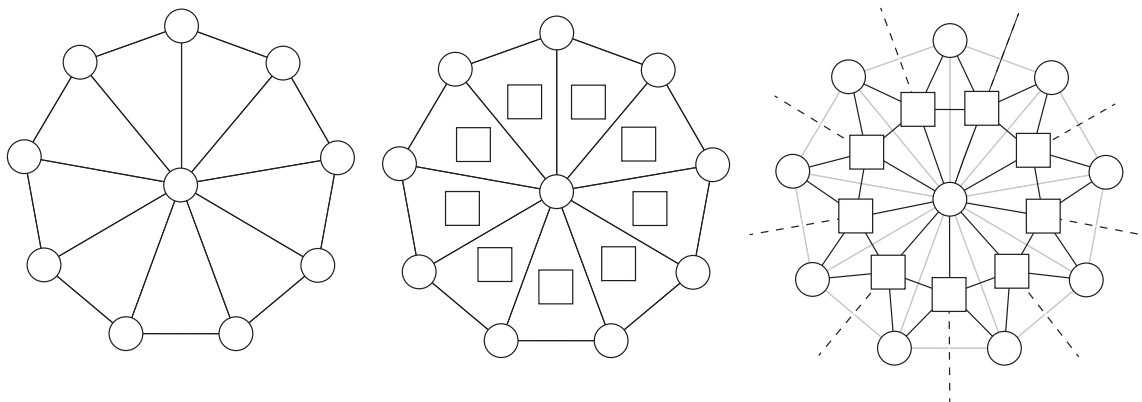
Figure 4: Left: A triangular patch with vertices illustrated by circles. Middle: face vertices are inserted in each triangle. Right: new edges are inserted (black lines) and old edges are removed (grey lines). Dashed lines connect a face-vertex to an adjacent triangle.

prove to reduce to width one when the appropriate equations for width two are formed (the other ring of a_i values all turn out to be zero). We indicate why this happens at the end of Section 5. As a result, here we only present the width-1 case of **A**.

4. $\sqrt{3}$ Subdivision: P Column Diagram

An important question corresponding to our construction is how to modify diagrams **P**, **A**, **Q**, and **B** such that extraordinary valences are handled. We begin by taking the definition of $\sqrt{3}$ subdivision [3] and composing a **P** column diagram for the subdivision. In $\sqrt{3}$ subdivision, a new vertex is inserted in the centroid of faces and existing vertices are averaged considering their neighborhoods. Finally, edges creating a coarse triangle are removed from the edge set of the fine model. Figure 4 shows the process of 1-to-3 refinement. The result for a central node of extraordinary valence, is shown in Figure 5. The key to understanding this diagram is that each n represents the valence of a node, and the α quantities, as defined in [3],

$$\alpha_{n_\lambda} = \frac{4 - 2\cos\left(\frac{2\pi}{n_\lambda}\right)}{9},$$

(4.1)

with λ standing for any of the circle-node indices.

The central node in Figure 5 has valence 9 to show an extraordinary example. Any node representing a displaced point (circle) may have any valence, and so, the grey triangles hide one or
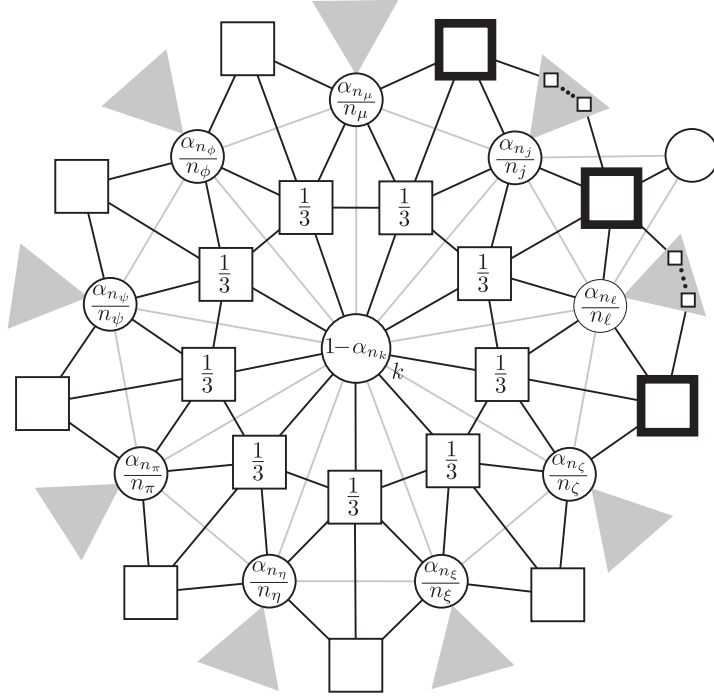
12

Figure 5: **P** column diagram $\mathbf{p}_k$ for $c_\kappa \to f_k$.

more edges. The connectivity graph of the fine mesh consists of the black edges, the grey triangles, and the circle and square nodes. Grey edges not being part of the connectivity graph, are also shown to reveal the connectivities between the original coarse nodes. Every other circle node in the fine mesh serves as the central node for a similar **P** column diagram, and what we establish with respect to Figure 5 will hold throughout.

The $\sqrt{3}$ subdivision generates the introduced points with a regular connectivity. Each introduced node is 6-connected, and its adjacent neighbors alternate between introduced-point nodes (squares) and displaced-point nodes (circles). As a consequence of this, for $\sqrt{3}$ subdivision, the three nodes at the upper right edge of Figure 5, distinguished by bold squares, are joined through a chain of square nodes, and no circle nodes, as indicated by the two mini-chains of square nodes within the two upper-right grey triangles. It turns out that this subdivision-induced regularity, even after just one step of the subdivision, will permit us to develop a multiresolution for generally-connected coarse meshes.

13

5. $\sqrt{3}$ Reversal: A Row Diagram

To reverse the $\sqrt{3}$ subdivision, we find an **A** row diagram for each coarse node (displaced fine node). Figure 6 shows how such a diagram appears if it has *width* 1. By default, the local least squares construction begins with a diagram of width 2, to include all fine points influenced by the central node of Figure 5, but, as it will be made clear at the end of this section, equations (3.3) can sometimes act to zero out the outermost elements of **A**, and that is exactly what happens in $\sqrt{3}$ subdivision, so that Figure 6 is sufficient for our purposes.
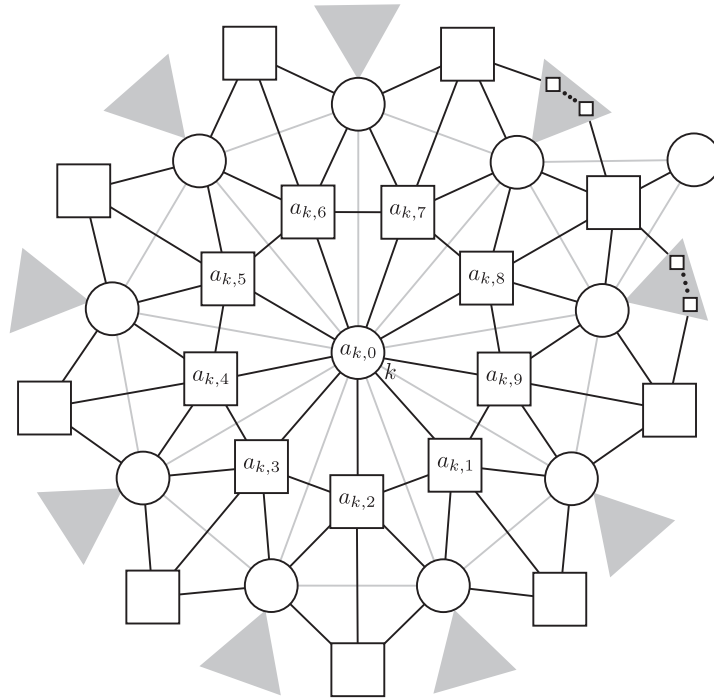
Figure 6: **A** row diagram $\mathbf{a}_k$ to obtain c_κ.

To repeat (3.3), the row-column interaction between the central a values of Figure 6 and the central column p values represented by Figure 5 must result in 1:

$$(1 - \alpha_{n_k})a_{k,0} + \frac{1}{3}a_{k,1} + \cdots + \frac{1}{3}a_{k,9} = 1.$$

The row-column interaction between the a values of Figure 6 and the p values of any of the peripheral
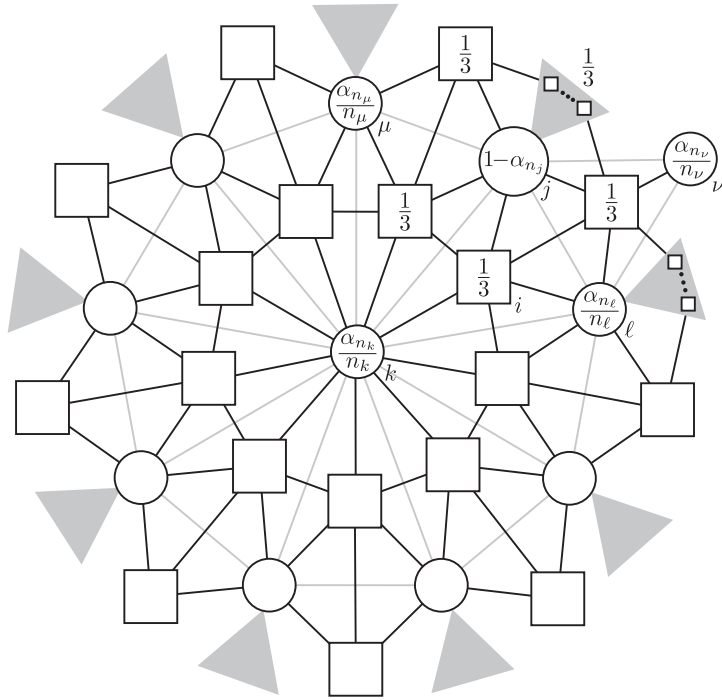
14

Figure 7: **P** Column on the periphery.

coarse nodes, e.g., those in Figure 7, must result in 0:

$$\frac{\alpha_{n_k}}{n_k}a_{k,0} + 0a_{k,1} + \cdots + 0a_{k,\lambda-1} + \frac{1}{3}a_{k,\lambda} + \frac{1}{3}a_{k,\lambda+1} + 0a_{k,\lambda+2} + \cdots + 0a_{k,9} = 0.$$

15

It is more informative to put this in terms of the submatrix of $\mathbf{P}$ corresponding to these equations:

$$[a_{k,0}, a_{k,1}, \ldots, a_{k,9}] \begin{bmatrix} 1-\alpha_{n_k} & \frac{\alpha_{n_k}}{n_k} & \frac{\alpha_{n_k}}{n_k} & \frac{\alpha_{n_k}}{n_k} & \frac{\alpha_{n_k}}{n_k} & \frac{\alpha_{n_k}}{n_k} & \frac{\alpha_{n_k}}{n_k} & \frac{\alpha_{n_k}}{n_k} & \frac{\alpha_{n_k}}{n_k} & \frac{\alpha_{n_k}}{n_k} \\ \frac{1}{3} & \frac{1}{3} & 0 & 0 & 0 & 0 & 0 & 0 & 0 & \frac{1}{3} \\ \frac{1}{3} & \frac{1}{3} & \frac{1}{3} & 0 & 0 & 0 & 0 & 0 & 0 & 0 \\ \frac{1}{3} & 0 & \frac{1}{3} & \frac{1}{3} & 0 & 0 & 0 & 0 & 0 & 0 \\ \frac{1}{3} & 0 & 0 & \frac{1}{3} & \frac{1}{3} & 0 & 0 & 0 & 0 & 0 \\ \frac{1}{3} & 0 & 0 & 0 & \frac{1}{3} & \frac{1}{3} & 0 & 0 & 0 & 0 \\ \frac{1}{3} & 0 & 0 & 0 & 0 & \frac{1}{3} & \frac{1}{3} & 0 & 0 & 0 \\ \frac{1}{3} & 0 & 0 & 0 & 0 & 0 & \frac{1}{3} & \frac{1}{3} & 0 & 0 \\ \frac{1}{3} & 0 & 0 & 0 & 0 & 0 & 0 & \frac{1}{3} & \frac{1}{3} & 0 \\ \frac{1}{3} & 0 & 0 & 0 & 0 & 0 & 0 & 0 & \frac{1}{3} & \frac{1}{3} \end{bmatrix} = [1, 0, \ldots, 0].$$

(5.1)

The matrix in equation (5.1) is the version for $n_k = 9$, which has 10 columns and 10 rows. Generally, for a node with n_k-connectivity, the matrix will have n_k+1 rows and columns, and the pattern of the contents in each column follows what is shown in (5.1) which is equivalent to the local subdivision matrix of [3].

The minimum norm solutions (3.3) in all cases follow a simple pattern. If the central node has n_k-connectivity as in Figure 5, then

$$a_{k,0} = -\frac{2}{3\alpha_{n_k} - 2} \tag{5.2}$$

and

$$a_{k,i} = \frac{3}{n_k} \cdot \frac{\alpha_{n_k}}{3\alpha_{n_k} - 2} \tag{5.3}$$

for $i > 2$. For example, the first condition of (3.3) can be easily verified using (5.2) and (5.3) for $\mathbf{P}$ and $\mathbf{A}$ diagrams. From here on, for simplicity, we will let a_k stand for the value of $a_{k,0}$ of (5.2) and h_k stand for the common value of all other $a_{k,i}$ of (5.3).

We end this section by seeing why the outer ring of $\mathbf{A}$ components are zero. Figure 8 looks at corresponding portions of Figure 6 and Figure 5, with Figure 6 filled out to width 2. The interaction

16

between the shown portions of these diagrams, for the purpose of constructing $\mathbf{A}$, would yield

$$a_{k,10}\frac{\alpha_{n_j}}{n_j} + a_{k,11}\frac{\alpha_{n_\ell}}{n_\ell} = 0.$$

Continuing around the margin of the $\mathbf{A}$ diagram in Figure 6 (filling in unknowns $a_{k,12},\ldots,a_{k,18}$) yields a set of similar equations that can be expressed in matrix form as

$$[a_{k,10},\ldots,a_{k,18}]\begin{bmatrix} \frac{\alpha_{n_j}}{n_j} & 0 & 0 & 0 & 0 & 0 & 0 & 0 & \frac{\alpha_{n_j}}{n_j} \\ \frac{\alpha_{n_\ell}}{n_\ell} & \frac{\alpha_{n_\ell}}{n_\ell} & 0 & 0 & 0 & 0 & 0 & 0 & 0 \\ 0 & \frac{\alpha_{n_\zeta}}{n_\zeta} & \frac{\alpha_{n_\zeta}}{n_\zeta} & 0 & 0 & 0 & 0 & 0 & 0 \\ 0 & 0 & \frac{\alpha_{n_\xi}}{n_\xi} & \frac{\alpha_{n_\xi}}{n_\xi} & 0 & 0 & 0 & 0 & 0 \\ 0 & 0 & 0 & \frac{\alpha_{n_\eta}}{n_\eta} & \frac{\alpha_{n_\eta}}{n_\eta} & 0 & 0 & 0 & 0 \\ 0 & 0 & 0 & 0 & \frac{\alpha_{n_\pi}}{n_\pi} & \frac{\alpha_{n_\pi}}{n_\pi} & 0 & 0 & 0 \\ 0 & 0 & 0 & 0 & 0 & \frac{\alpha_{n_\psi}}{n_\psi} & \frac{\alpha_{n_\psi}}{n_\psi} & 0 & 0 \\ 0 & 0 & 0 & 0 & 0 & 0 & \frac{\alpha_{n_\phi}}{n_\phi} & \frac{\alpha_{n_\phi}}{n_\phi} & 0 \\ 0 & 0 & 0 & 0 & 0 & 0 & 0 & \frac{\alpha_{n_\mu}}{n_\mu} & \frac{\alpha_{n_\mu}}{n_\mu} \end{bmatrix} = [0,\ldots,0].$$

The structure of the matrix for any other number of outer-ring $\mathbf{A}$ components is consistent with this. The rows of the matrix clearly have linear independence, and left-multiplication by the $\mathbf{a}$ vector forms a linear combination of those rows. The result is zero only when $a_{k,10} = \cdots = a_{k,18} = 0$.

6. $\sqrt{3}$ Correction: Q Column Diagram

Finding corrections $\mathbf{e}$ (3.6) from detail information $\mathbf{d}$ (3.5) is done using the matrix $\mathbf{Q}$, which is constructed one column at a time, as discussed in [1]. The ith column of $\mathbf{Q}$ governs the contribution to $\mathbf{e}$ made by the detail d_i on the introduced (square) node i, and there is one column of $\mathbf{Q}$ uniquely associated with each introduced node; e.g., see Figure 9. That node, and certain surrounding nodes, are labeled with symbols for a $\mathbf{Q}$ column diagram of width 1. One usually starts with a trial diagram of width 0 (the node i alone in this case), and increases the width until a diagram is found for which all possible interactions with the row diagrams of $\mathbf{A}$ will be zero. For the $\sqrt{3}$ subdivision, width 1 proves to be sufficient.
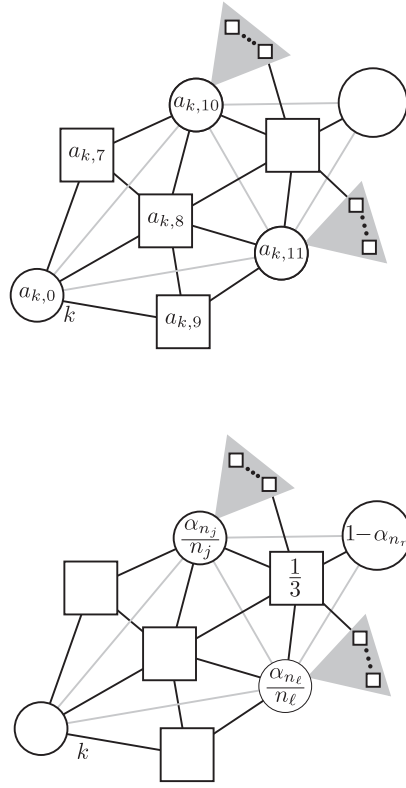
17

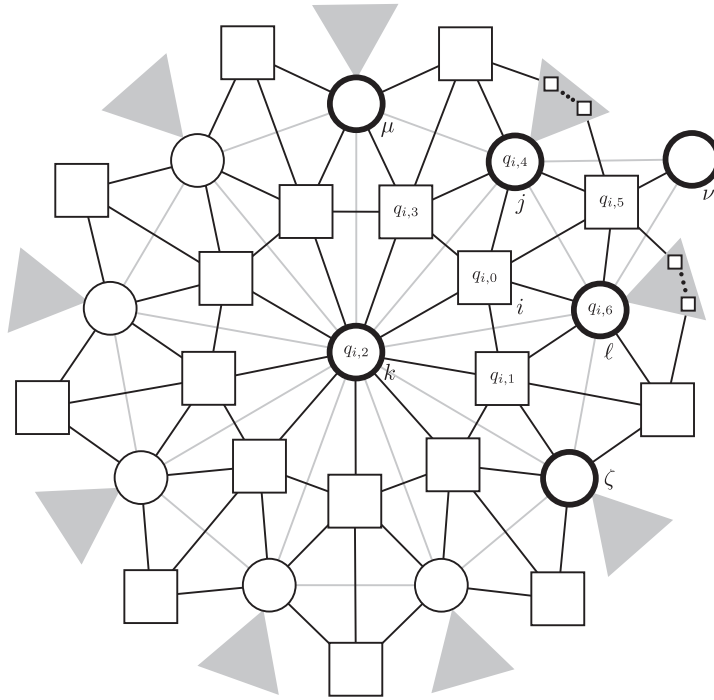Figure 8: Row diagram of $\mathbf{A}$, interacting with an outer $\mathbf{P}$ column diagram.

Figure 9: The **Q** column diagram for node i.

Recall that we have found **A** row diagrams to consist of a displaced coarse (circular) node as a central node, with one value, together with all its immediately surrounding introduced (square) nodes, with a commonly held value, namely,

$$a_\sigma = -\frac{2}{3\alpha_{n_\sigma} - 2}, \text{and} \tag{6.1}$$

$$h_\sigma = \frac{3}{n_\sigma} \frac{\alpha_{n_\sigma}}{3\alpha_{n_\sigma} - 2}. \tag{6.2}$$

And this is the case for the emphasized nodes ($\sigma = \mu, j, \nu, k, \ell, \zeta$) in Figure 9. These are the central nodes of all the **A** row diagrams that will interact with the proposed **Q** column diagram, and the

19

requirement is that these interactions be as in equation (6.3) for nontrivial values of $q_{i,j}$, $j = 0, \ldots, 6$:

$$
\begin{bmatrix}
h_k & h_k & a_k & h_k & 0 & 0 & 0 \\
0 & h_\zeta & 0 & 0 & 0 & 0 & 0 \\
0 & 0 & 0 & h_\mu & 0 & 0 & 0 \\
h_j & 0 & 0 & h_j & a_j & h_j & 0 \\
0 & 0 & 0 & 0 & 0 & h_\nu & 0 \\
h_\ell & h_\ell & 0 & 0 & 0 & h_\ell & a_\ell
\end{bmatrix}
\begin{bmatrix}
q_{i,0} \\
q_{i,1} \\
q_{i,2} \\
q_{i,3} \\
q_{i,4} \\
q_{i,5} \\
q_{i,6}
\end{bmatrix}
=
\begin{bmatrix}
0 \\
0 \\
0 \\
0 \\
0 \\
0 \\
0
\end{bmatrix}.
\tag{6.3}
$$

This is equivalent to demanding that the $\mathbf{q}_i$ vector of (6.3) lie in the null space of the coefficient matrix in (6.3). The null space of this matrix has dimension one, and a corresponding basis vector is

$$
\begin{bmatrix}
1 \\
0 \\
-\dfrac{h_k}{a_k} \\
0 \\
-\dfrac{h_j}{a_j} \\
0 \\
-\dfrac{h_\ell}{a_\ell}
\end{bmatrix}.
\tag{6.4}
$$

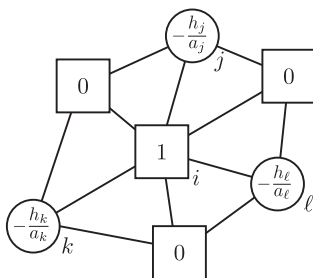Transcribing this to a diagram, we arrive at Figure 10.

Figure 10: $\mathbf{Q}$ column diagram.

20

To apply $\mathbf{Q}$, we must have detail vectors d assigned to each introduced (square) node. The elements of $\mathbf{Q}$ will be used to compute the errors $\mathbf{e}$ as follows: each of the diagram's node values in Figure 10 specifies what multiple of the d_i associated with the central node i is added onto the diagram node's accumulating e value. For instance, $-\frac{h_k}{a_k} \times d_i$ is added to node k as node i's contribution to e_k. When every square node has been visited, and all multiples have been accumulated, we have the error on the ith square node as

$$e_i = d_i \tag{6.5}$$

and the error on the kth circle node as

$$e_k = -\frac{h_k}{a_k} \sum_{\lambda=1}^{n_k} d_{k+\lambda}, \tag{6.6}$$

where a_k and h_k are the $\mathbf{A}$ values associated with the k circle node, and the $d_{k+\lambda}$ are the details associated with all the n_k square nodes immediately surrounding that circle node. Plugging h_k and a_k of equations 6.1 and 6.2 in this equation, we obtain:

$$e_k = \frac{3\alpha_{n_k}}{2n_k} \sum_{\lambda=1}^{n_k} d_{k+\lambda} \tag{6.7}$$

With this insight, we could suspend the construction at this point, since we see that the $\mathbf{d}$ values on the introduced (square) nodes are simply the error values on those nodes, which we can calculate as the simple differences $\mathbf{P\bar{c}} - \mathbf{g}$, and the error values on the displaced (circular) nodes are simple combinations of those introduced-node errors. However, to be complete, we will construct the $\mathbf{B}$ filter in the next section.

7. $\sqrt{3}$ Detail: B Row Diagram

$\mathbf{B}$ is used to compute the detail value d_i for each introduced (square) node i to be used with column $\mathbf{q}_i$ of $\mathbf{Q}$ to ascertain the errors shown in (3.4). $\mathbf{B}$ can be found in two steps [1]. First, a left inverse $\mathbf{T}$ is found for $\mathbf{Q}$:

$$\mathbf{TQ} = \mathbf{I}.$$

This is done via *local least squares* just as $\mathbf{A}$ was found from $\mathbf{P}$. Then, $\mathbf{B}$ is obtained as

$$\mathbf{B} = \mathbf{T}\left(\mathbf{I} - \mathbf{PA}\right). \tag{7.1}$$

21

In particular, the ith row, $\mathbf{b_i}$ of $\mathbf{B}$, will be obtained from $\mathbf{T}$, $\mathbf{P}$ and $\mathbf{A}$ through t_i, the ith row of $\mathbf{T}$, and the intermediate rows $\mathbf{r}_i$ and $\mathbf{s}_i$ as follows:

$$
\begin{aligned}
\mathbf{r}_i &= \mathbf{t}_i \mathbf{P} \\
\mathbf{s}_i &= \mathbf{r}_i \mathbf{A} \\
\mathbf{b}_i &= \mathbf{t}_i - \mathbf{s}_i.
\end{aligned}
\tag{7.2}
$$

The construction of $\mathbf{T}$ turns out to be trivial for the $\mathbf{Q}$ we have determined in Section 6. Figure 11 shows the $\mathbf{T}$ row diagram of width 1 for node i. Compare this with Figure 10 for the $\mathbf{Q}$ column diagram for the same node, and the $\mathbf{TQ}$ interaction is easily seen. The sum of the products
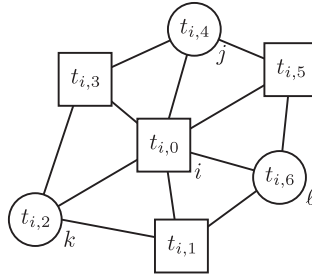

Figure 11: Width 1 $\mathbf{t}_i$.

of the node entries in Figure 10 and Figure 11 must add up to 1, and the sum of the products of the quantities $t_{i,0}, \ldots, t_{i,6}$ with any other $\mathbf{Q}$ column diagram must be 0. This leads to

$$
[\, t_{i,0}\ t_{i,1}\ t_{i,2}\ t_{i,3}\ t_{i,4}\ t_{l,5}\ t_{i,6}\,]
\begin{bmatrix}
1 & 0 & 0 & 0 & 0 & 0 & 0 \\
0 & 1 & 0 & 0 & 0 & 0 & 0 \\
-\frac{h_k}{a_k} & -\frac{h_k}{a_k} & -\frac{h_k}{a_k} & 0 & 0 & 0 & 0 \\
0 & 0 & 0 & 1 & 0 & 0 & 0 \\
-\frac{h_j}{a_j} & 0 & 0 & -\frac{h_j}{a_j} & -\frac{h_j}{a_j} & -\frac{h_j}{a_j} & 0 \\
0 & 0 & 0 & 0 & 0 & 1 & 0 \\
-\frac{h_\ell}{a_\ell} & -\frac{h_\ell}{a_\ell} & 0 & 0 & 0 & -\frac{h_\ell}{a_\ell} & -\frac{h_\ell}{a_\ell}
\end{bmatrix}
= [\, 1\ 0\ 0\ 0\ 0\ 0\ 0\,],
\tag{7.3}
$$

in which duplicate columns have been removed. If there is no solution, then we proceed to a wider $\mathbf{T}$ diagram. If there is a unique solution, then we use it. If there are many solutions, then we use

22

the one of least Euclidean norm. There is, in fact, one solution given by

$$t_{i,0} = 1 \quad \text{and} \quad t_{i,1} = \cdots = t_{i,6} = 0 \ . \tag{7.4}$$

Referring to (7.2), our next task is to find $\mathbf{r}_i$. Expressed as diagrams, we are interested in all the $\mathbf{P}$ column diagrams that have a nontrivial overlap with the $\mathbf{T}$ row diagram of Figure 11. Figure 12 shows one such interaction. The result of the row-column multiplication depicted in Figure 12 will
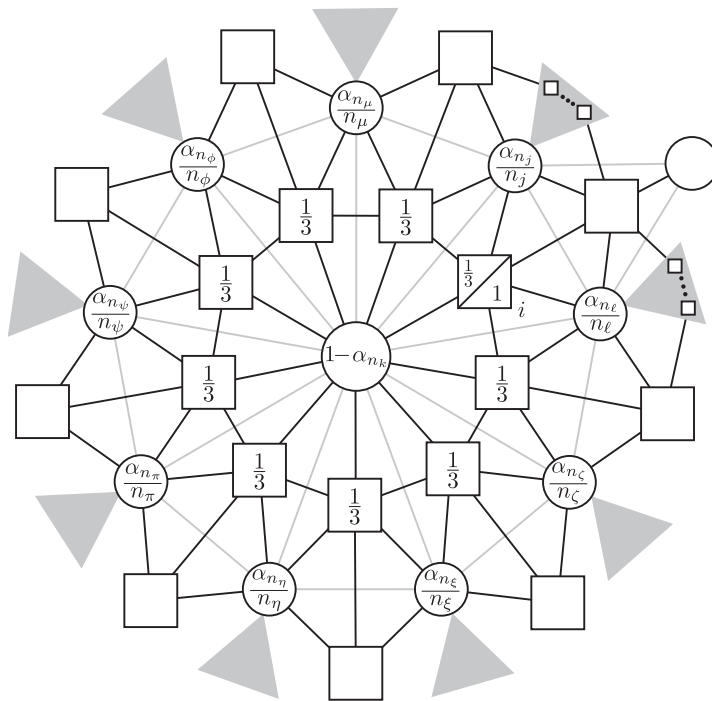

Figure 12: The $\mathbf{t}_i$ row diagram interacting with the $\mathbf{p}_k$ column diagram.

be $\frac{1}{3}$, and this will appear as one element of the $\mathbf{r}_i$ row diagram, referring to the equations (7.2). The proper node on which to write this value is the central (circle) node associated with the column of $\mathbf{P}$ that participated in this interaction. Continuing, we arrive at the row diagram for $\mathbf{r}_i$ as shown in Figure 13 with $r_{i,0} = 0, r_{i,1} = 0, r_{i,0} = 0, r_{i,2} = \frac{1}{3}, r_{i,3} = 0, r_{i,4} = \frac{1}{3}, r_{i,5} = 0, r_{i,6} = \frac{1}{3}$.

The final step is to form the row diagram for $\mathbf{s}_i$ given in (7.2). It will be formed by the $\mathbf{r}_i$ of Figure 13 interacting with all possible $\mathbf{A}$ diagrams, which will be

$$\frac{1}{3}\mathbf{a}_k + \frac{1}{3}\mathbf{a}_j + \frac{1}{3}\mathbf{a}_\ell \ . \tag{7.5}$$
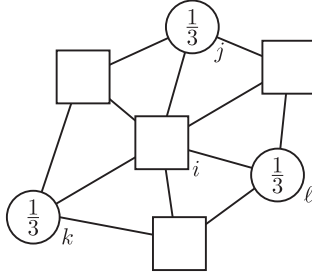
23

Figure 13: The row diagram for $\mathbf{r}_i$.

The final step in (7.2) consists merely of subtracting the row diagram of (7.5) from the row diagram of Figure 11. The result is shown in Figure 14, where

$$
\begin{aligned}
w_{kj} &= -\frac{h_k + h_j}{3} \\
w_{k\ell} &= -\frac{h_k + h_\ell}{3} \\
w_{j\ell} &= -\frac{h_j + h_\ell}{3} \\
w_{kj\ell} &= 1 - \frac{h_k + h_j + h_\ell}{3}.
\end{aligned}
\tag{7.6}
$$

The diagram of Figure 14 looks more complicated than it really is. Node i will be at the centroid of a triangle joining 3 circle nodes. Each of those circle nodes will be the central node for an **A** diagram. To obtain the **B** diagram, simply put a 1 on the square node i and then subtract $\frac{1}{3}$ times each of the 3 circle-node **A** diagrams. The **B** diagram is the resulting row diagram. To use the diagram of Figure 14 to compute the detail coordinates on the i square node, take each value written on a node in the figure, multiply that value by the fine point coordinates associated with that node, and sum up the results.

The action of the $\mathbf{b}_i$ row diagram of **B** can be interpreted as the process of reversing the subdivision to estimate the coarse position of each of the three circle nodes adjoining a square node, followed by applying the subdivision to these estimated coarse circle positions ($\frac{1}{3}$ and $\frac{1}{3}$ and $\frac{1}{3}$) to create the "subdivision version" of the introduced square node, and finally subtracting that from the actual position of the square node. And that is, in words, the description of how the error associated with the square node would be produced, as we mentioned at the end of Section 6.
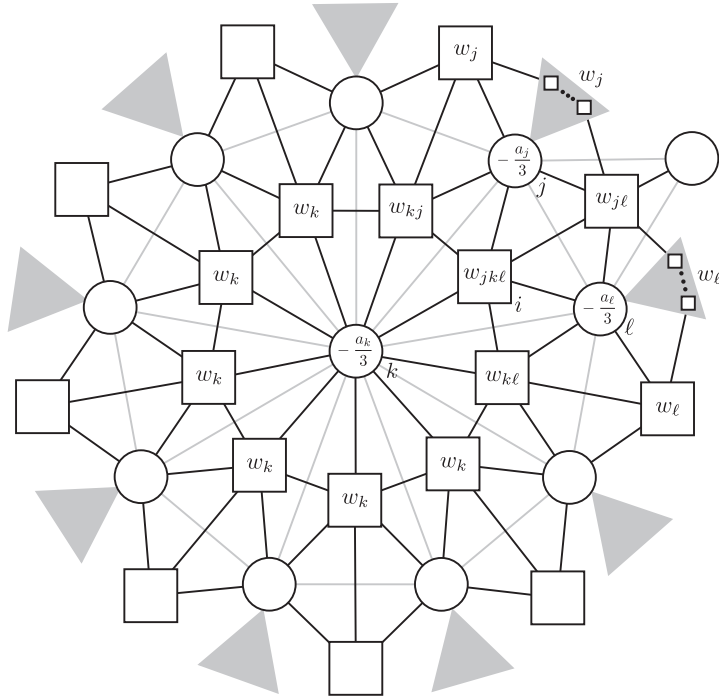
24

Figure 14: The row diagram for **B**.

8. Loop and Catmull-Clark Schemes

In previous sections, we explained how to set up necessary matrices for the case of $\sqrt{3}$ subdivision in details. In this section, we briefly describe how to extend the method of $\sqrt{3}$ subdivision for other subdivision schemes. To show the feasibility of this task, we show the equivalent matrix for the system (5.1) for the case of Loop and Catmull-Clark subdivision schemes and provide the reversal filter that is the result of solving that equation.

Using the approach of Section 5 on the Loop subdivision (see Figure 15 for Loop's general diagram), the corresponding matrix of (5.1) turns out to be (here for valence 7 and corresponding
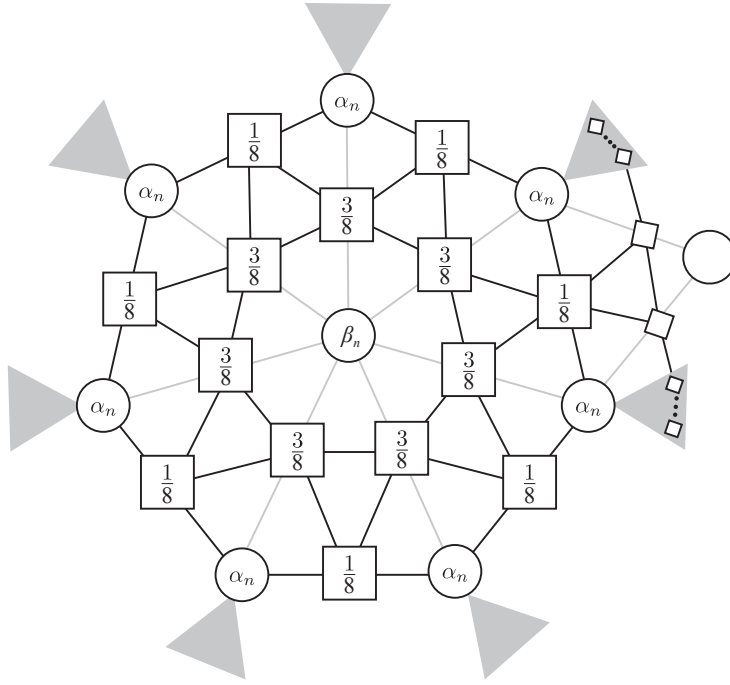
Figure 15: **P** column diagram for the Loop subdivision.

larger versions for higher valences):

$$\mathbf{P} = \begin{bmatrix} \beta_n & \alpha_n & \alpha_n & \alpha_n & \alpha_n & \alpha_n & \alpha_n & \alpha_n \\ 3/8 & 3/8 & 1/8 & 0 & 0 & 0 & 0 & 1/8 \\ 3/8 & 1/8 & 3/8 & 1/8 & 0 & 0 & 0 & 0 \\ 3/8 & 0 & 1/8 & 3/8 & 1/8 & 0 & 0 & 0 \\ 3/8 & 0 & 0 & 1/8 & 3/8 & 1/8 & 0 & 0 \\ 3/8 & 0 & 0 & 0 & 1/8 & 3/8 & 1/8 & 0 \\ 3/8 & 0 & 0 & 0 & 0 & 1/8 & 3/8 & 1/8 \\ 3/8 & 1/8 & 0 & 0 & 0 & 0 & 1/8 & 3/8 \end{bmatrix}.$$

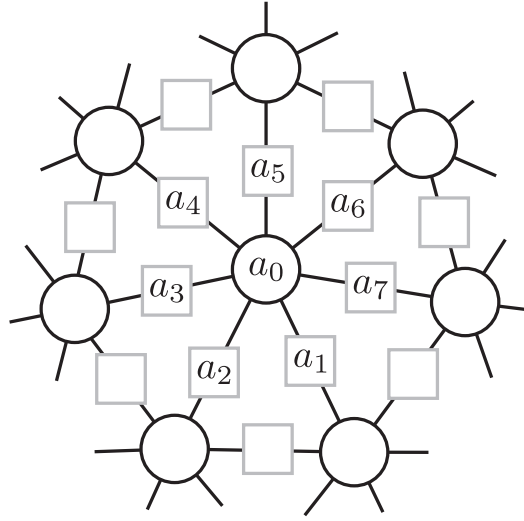The solution **A** filter has

$$a_0 = \frac{-5}{3n\alpha_n - 5\beta_n}$$

26

Figure 16: **A** for Loop subdivision at an extraordinary point.

and

$$a_i = \frac{8\alpha_n}{3n\alpha_n - 5\beta_n}, \text{ for } i = 1, ..., n,$$

where α_n is as given by Loop for the extraordinary point of valence n, and $\beta_n = 1 - n\alpha_n$ (see Figure 16 for the placement of the a values for the valence 7 example).

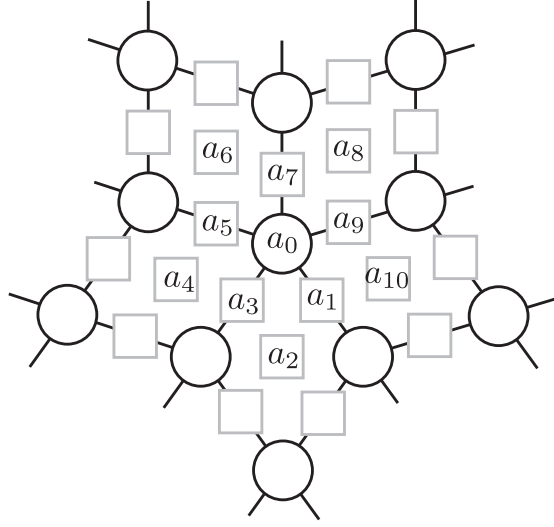Taking the same approach on the Catmull-Clark subdivision, the corresponding matrix of (5.1)

27

Figure 17: **A** for Catmull-Clark at an extraordinary point.

is (here for valence 5 and correspondingly for larger versions):

$$
\mathbf{P} =
\begin{bmatrix}
\mathcal{A} & \mathcal{B} & \mathcal{C} & \mathcal{B} & \mathcal{C} & \mathcal{B} & \mathcal{C} & \mathcal{B} & \mathcal{C} & \mathcal{B} & \mathcal{C} \\
3/8 & 3/8 & 1/16 & 1/16 & 0 & 0 & 0 & 0 & 0 & 1/16 & 1/16 \\
1/4 & 1/4 & 1/4 & 1/4 & 0 & 0 & 0 & 0 & 0 & 0 & 0 \\
3/8 & 1/16 & 1/16 & 3/8 & 1/16 & 1/16 & 0 & 0 & 0 & 0 & 0 \\
1/4 & 0 & 0 & 1/4 & 1/4 & 1/4 & 0 & 0 & 0 & 0 & 0 \\
3/8 & 0 & 0 & 1/16 & 1/16 & 3/8 & 1/16 & 1/16 & 0 & 0 & 0 \\
1/4 & 0 & 0 & 0 & 0 & 1/4 & 1/4 & 1/4 & 0 & 0 & 0 \\
3/8 & 0 & 0 & 0 & 0 & 1/16 & 1/16 & 3/8 & 1/16 & 1/16 & 0 \\
1/4 & 0 & 0 & 0 & 0 & 0 & 0 & 1/4 & 1/4 & 1/4 & 0 \\
3/8 & 1/16 & 0 & 0 & 0 & 0 & 0 & 1/16 & 1/16 & 3/8 & 1/16 \\
1/4 & 1/4 & 0 & 0 & 0 & 0 & 0 & 0 & 0 & 1/4 & 1/4
\end{bmatrix} ,
$$

where $\mathcal{A} = \frac{4n-7}{4n}$, $\mathcal{B} = \frac{3}{2n^2}$, and $\mathcal{C} = \frac{1}{4n^2}$. The solution $\mathbf{A}$ filter has

$$a_0 = \frac{n}{n-3}$$

and

$$a_{2i+1} = \frac{-4}{n(n-3)}, \text{ for } i = 0, 1, 2, \ldots$$

and

$$a_{2j} = \frac{1}{n(n-3)}, \text{ for } j = 1, 2, \ldots$$

(see Figure 17 for the placement of the a values for the valence 5 example).

9. Boundary Curves

Boundary curves are important for subdivision surfaces as they can be used to represent sharp features, creases, and corners or handle boundaries of an open mesh. In this section, we discuss how we can apply our proposed diagrammatic approach for boundary curves on a $\sqrt{3}$ subdivision surface.

In [3], boundary points are handled separately where coarse points on the boundary are treated as if they were the coefficients of a cubic B-spline with uniform knots, let's say with 3 units of spacing per knot:

$$\ldots \quad 10 \quad 13 \quad 16 \quad 19 \ldots$$

and the uniform insertion of two knots per existing knot interval is employed; that is,

$$\ldots \ 10 \ 11 \ 12 \ 13 \ 14 \ 15 \ 16 \ 17 \ 18 \ 19 \ \ldots,$$

to transform the coarse boundary points into the fine ones. This results in filters

$$\frac{1}{27} \left[1, 4, 10, 16, 19, 16, 10, 4, 1 \right],$$

which corresponds, in our terms, to the $\mathbf{P}$ diagram shown in Figure 18. Figure 19 illustrates an example of a closed sharp feature on a mesh.

Diagrams for B-splines have been developed in, for example, [13, 30]. It is straightforward to establish the corresponding $\mathbf{A}$, $\mathbf{B}$ and $\mathbf{Q}$ diagrams for the $\mathbf{P}$ of Figure 18.

Of course, as before, $\mathbf{A}$ reverses $\mathbf{P}$ to recover $\mathbf{c}$ from $\mathbf{f}$. But, if the fine points are data points or perturbed subdivision points, $\mathbf{g}$, then $\mathbf{A}$ produces only approximate coarse points $\bar{\mathbf{c}}$, and we
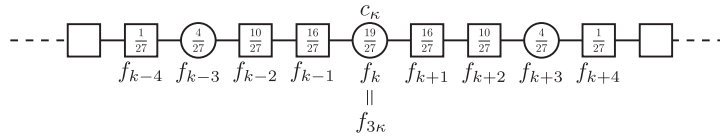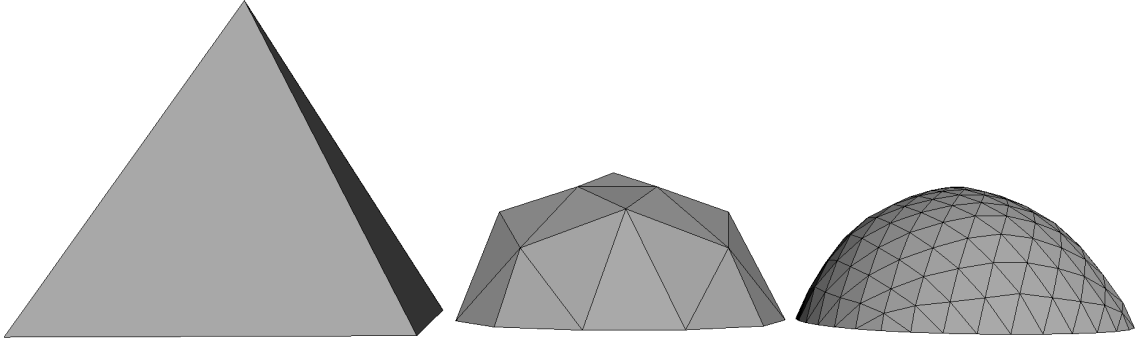
29

Figure 18: The boundary **P** diagram.

Figure 19:   The result of subdivision on a closed boundary sharp feature on a mesh.

would like to find **B** and **Q** to express error information. The appropriate **A** diagram is shown in Figure 20. This diagram corresponds to recovering the location of the coarse point c_κ from its displaced image $f_k = f_{3\kappa}$ as

$$c_\kappa = \sum_{\lambda=k-4}^{k+4} a_\lambda f_\lambda,$$

with the coefficient a_λ standing for the fraction shown on node f_λ.

If the situation immediately above is switched from subdivision points **f** to data or perturbed points **g**, which switches the recovered coarse points **c** to approximate coarse points $\bar{\mathbf{c}}$, then we need **B** and **Q**. The appropriate **B** diagrams (there are two) are shown in Figure 21. The b values are available in Appendix A.

The first diagram corresponds to computing the detail coordinates associated with $g_{3\kappa-1} = g_{k-1}$ as

$$d_{k-1} = \sum_{\lambda=-7}^{+4} b_{5-\lambda} g_{k+\lambda},$$

and the second diagram corresponds to computing the detail coordinates associated with $g_{3\kappa+1} =$
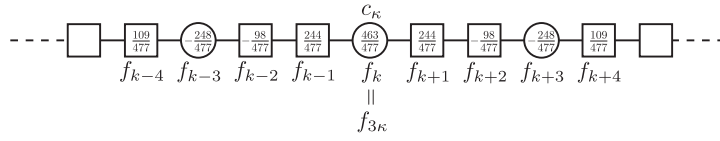
30

$$\begin{array}{c} c_\kappa \\ \cdots - \square - \boxed{\tfrac{109}{477}} - \big(\tfrac{248}{477}\big) - \boxed{\tfrac{98}{477}} - \boxed{\tfrac{244}{477}} - \big(\tfrac{463}{477}\big) - \boxed{\tfrac{244}{477}} - \boxed{\tfrac{98}{477}} - \big(\tfrac{248}{477}\big) - \boxed{\tfrac{109}{477}} - \square - \cdots \\ f_{k-4} \quad f_{k-3} \quad f_{k-2} \quad f_{k-1} \quad f_k \quad f_{k+1} \quad f_{k+2} \quad f_{k+3} \quad f_{k+4} \\ \| \\ f_{3\kappa} \end{array}$$

Figure 20: Boundary **A** diagram.

$$\bar{c}_\kappa$$
$$\cdots - b_{12} - (b_{11}) - b_{10} - b_9 - (b_8) - b_7 - b_6 - (b_5) - b_4 - b_3 - (b_2) - b_1 - \square - \bigcirc - \square - \cdots$$
$$g_{k-7} \ \ g_{k-6} \ \ g_{k-5} \ \ g_{k-4} \ \ g_{k-3} \ \ g_{k-2} \ \ g_{k-1} \ \ g_k \ \ g_{k+1} \ \ g_{k+2} \ \ g_{k+3} \ \ g_{k+4} \ \ g_{k+5} \ \ g_{k+6} \ \ g_{k+7}$$
$$\| \\ g_{3\kappa}$$

$$\bar{c}_\kappa$$
$$\cdots - \square - \bigcirc - \square - b_1 - (b_2) - b_3 - b_4 - (b_5) - b_6 - b_7 - (b_8) - b_9 - b_{10} - (b_{11}) - b_{12} - \cdots$$
$$g_{k-7} \ \ g_{k-6} \ \ g_{k-5} \ \ g_{k-4} \ \ g_{k-3} \ \ g_{k-2} \ \ g_{k-1} \ \ g_k \ \ g_{k+1} \ \ g_{k+2} \ \ g_{k+3} \ \ g_{k+4} \ \ g_{k+5} \ \ g_{k+6} \ \ g_{k+7}$$
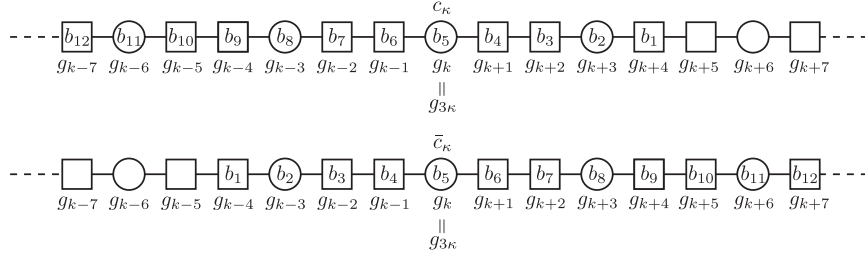$$\| \\ g_{3\kappa}$$

Figure 21: Boundary **B** diagrams.

g_{k+1} as

$$d_{k+1} = \sum_{\lambda=-4}^{+7} b_{5+\lambda} g_{k+\lambda}.$$

Finally, the appropriate **Q** diagrams (there are two) are shown in Figure 22. The q values are also
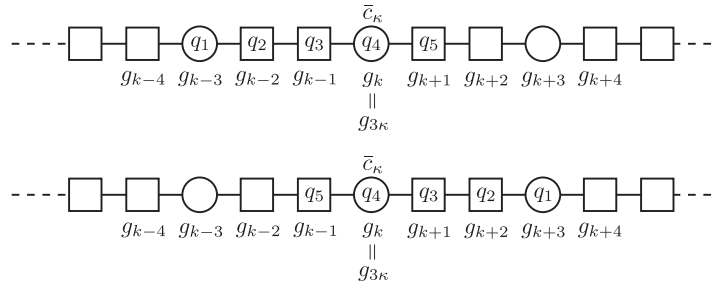
$$\bar{c}_\kappa$$
$$\cdots - \square - \square - (q_1) - q_2 - q_3 - (q_4) - q_5 - \square - \bigcirc - \square - \square - \cdots$$
$$g_{k-4} \ \ g_{k-3} \ \ g_{k-2} \ \ g_{k-1} \ \ g_k \ \ g_{k+1} \ \ g_{k+2} \ \ g_{k+3} \ \ g_{k+4}$$
$$\| \\ g_{3\kappa}$$

$$\bar{c}_\kappa$$
$$\cdots - \square - \square - \bigcirc - \square - q_5 - (q_4) - q_3 - q_2 - (q_1) - \square - \square - \cdots$$
$$g_{k-4} \ \ g_{k-3} \ \ g_{k-2} \ \ g_{k-1} \ \ g_k \ \ g_{k+1} \ \ g_{k+2} \ \ g_{k+3} \ \ g_{k+4}$$
$$\| \\ g_{3\kappa}$$

Figure 22: Boundary **Q** diagrams.

available in Appendix A.

These **Q** diagrams are column diagrams, and they translate into three distinct ways of computing the error of a fine point as follows:

1. for a *displaced point*, which corresponds to a circle node in Figure 22, we have, for example
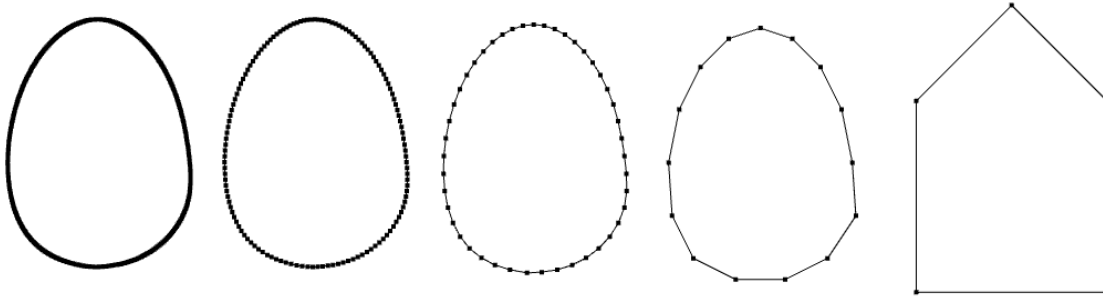
31

Figure 23: Applying ternary reverse subdivision on a curve.

for $g_{3\kappa} = g_k$,

$$e_k = q_1 d_{k-2} + q_4 d_{k-1} + q_4 d_{k+1} + q_1 d_{k+2},$$

where the d_j are the coordinates of the details on the nodes indicated by the subscripts;

2. for an *introduced point* preceding a displaced point, which corresponds to a square node to the left of a circle node in Figure 22, we have, for example for $g_{3\kappa-1} = g_{k-1}$,

$$e_{k-1} = q_2 d_{k-2} + q_3 d_{k-1} + q_5 d_{k+1};$$

3. for an introduced point following a displaced point, which corresponds to a square node to the right of a circle node in Figure 22, we have, for example for $g_{3\kappa+1} = g_{k+1}$,

$$e_{k+1} = q_5 d_{k-1} + q_3 d_{k+1} + q_2 d_{k+2}.$$

Figure 23 illustrates the reverse subdivision on a closed curve.

If a boundary curve is not closed and cyclic (see Figure 24), then we should be prepared to deal with end points. Kobbelt [3] ignores this possibility, but we have taken the trouble to provide **P**, **A**, **B** and **Q** for all cases from 4 up to 18 coarse points, at which juncture the interior boundary points may be treated as in figures 18 through 22. A cubic boundary curve, of course, must have at least 4 control vertices, hence giving the starting point of our work.

We use, as does Kobbelt, a cubic B-spline knot structure, and take

$$0, 0, 0, 0, 5, 8, 11, 14, \ldots \quad \text{knots every 3 integer positions onward}$$

for the beginning of the coarse boundary curve (and symmetrically at the end). We introduce new
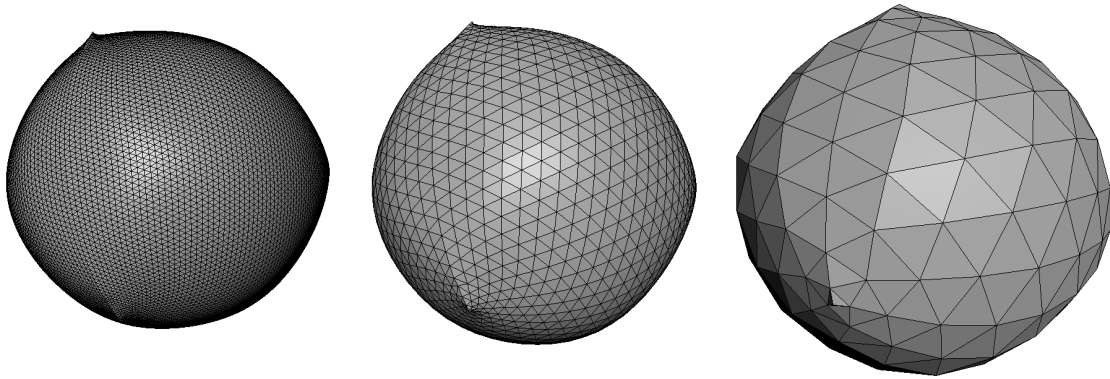
32

Figure 24: The result of subdivision on an open sharp feature on a mesh.

knots to obtain the knot structure

$$0, 0, 0, 0, 1, 2, 3, 4, 5, 6, 7, 8, 9, 10, 11, 12, 13, 14, \ldots \quad \text{knots every integer position onward}$$

for the fine boundary curve. The use of a quadruple knot at the beginning (and end) ensures that the curve's endpoints do not move in their spatial positions under the subdivision. Our choice of 5 as the first coarse knot thereafter, and of $1, 2, 3, 4$ as the knots introduced to transit to the sequence of fine knots, is based on trial and error to settle on what generally gave the most satisfying results. Additional matrices of $\mathbf{P}$, $\mathbf{B}$, $\mathbf{A}$, and $\mathbf{Q}$ for such boundary curves have been provided in the supplementary material.

10. Results

To validate our diagrammatic approach, we provide some results of the $\sqrt{3}$ multiresolution framework provided in our work here. The resulting $\mathbf{A}$ filters for the Loop and Catmull-Clark subdivisions are consistent with the ones previously constructed in [8, 9, 32]. To observe the result of our $\sqrt{3}$ multiresolution, we have applied its filters on a toroidal polyhedron whose vertices are obtained from sampling the parametric equation of a torus. Figure 25 illustrates the results of four iterations of reverse subdivisions of the toroidal polyhedron using the $\mathbf{A}$ mask. It is apparent that the proposed $\sqrt{3}$ multiresolution framework is quite stable.

To further establish the stability of our multiresolution, we have provided an example in which the vertices are randomly perturbed. In Figure 26, a toroidal polyhedron is once subdivided and
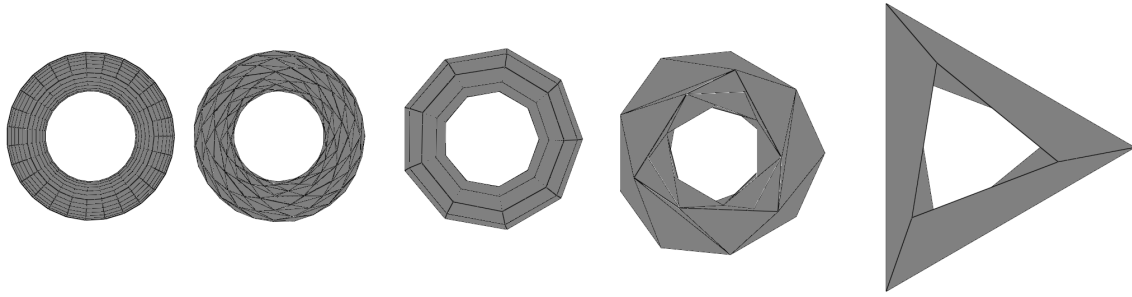
33

Figure 25: Three iterations of our decomposition applied on a toroidal polyhedron obtained from sampling the parametric equation of a torus.

then its vertices are randomly perturbed. As apparent in Figure 26, even when the input mesh of the multiresolution is not smooth, the result is quite satisfactory and stable.

Since all vertices in a toroidal polyhedron are regular, we need to examine our multiresolution for meshes with general connectivity. Figure 27 illustrates the reversing of the pawn model that has been subdivided twice using $\sqrt{3}$ subdivision. The original mesh is created by applying our reversal **A** mask twice as well.

In Figure 28, after two applications of $\sqrt{3}$ subdivision, we have randomly displaced some of the vertices to observe how stable our multiresolution performs when the geometry of the mesh is not obtained from the subdivision. We have initially decomposed the model into coarse vertices and details using the masks provided in **A** and **B** diagrams. We then reconstructed the same models by subdividing the coarse models and adding the necessary details using masks embedded in **P** and **Q** diagrams.
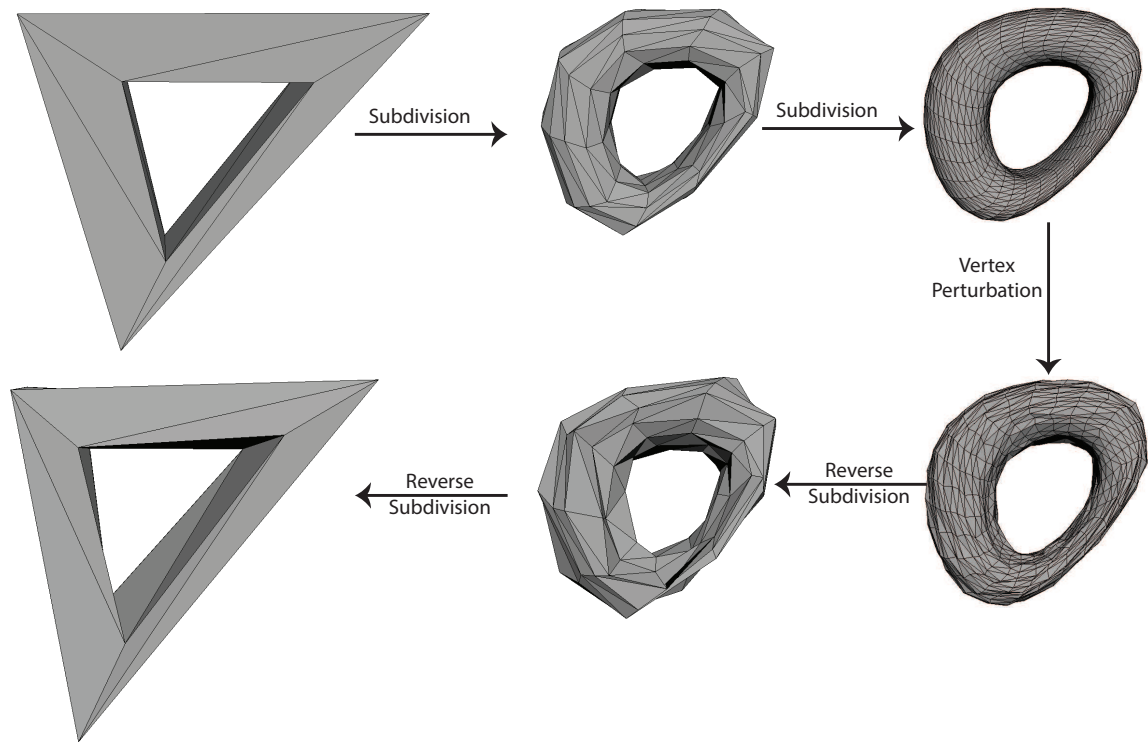
Figure 26: A toroidal polyhedron is subdivided and randomly perturbed. The perturbed model is then reversely subdivided and a mesh with the resolution of the original polyhedron is obtained.
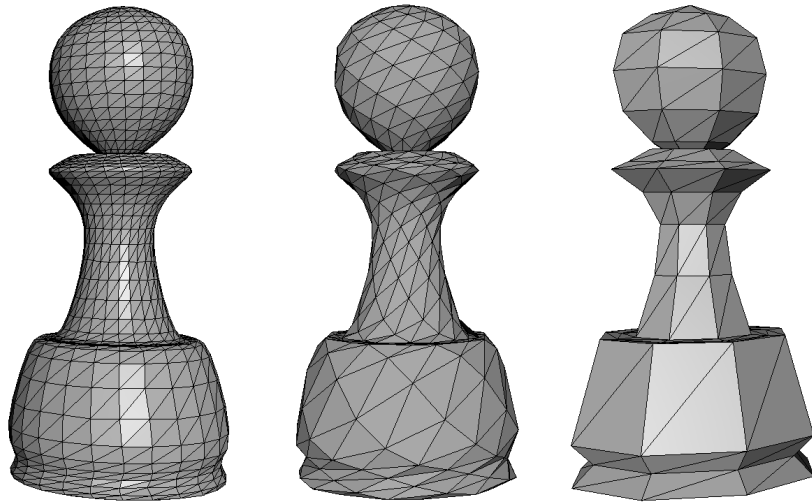
Figure 27: Decomposing a fine model that has been subdivided using $\sqrt{3}$ multiresolution twice. It is apparent that the original model is reconstructed.
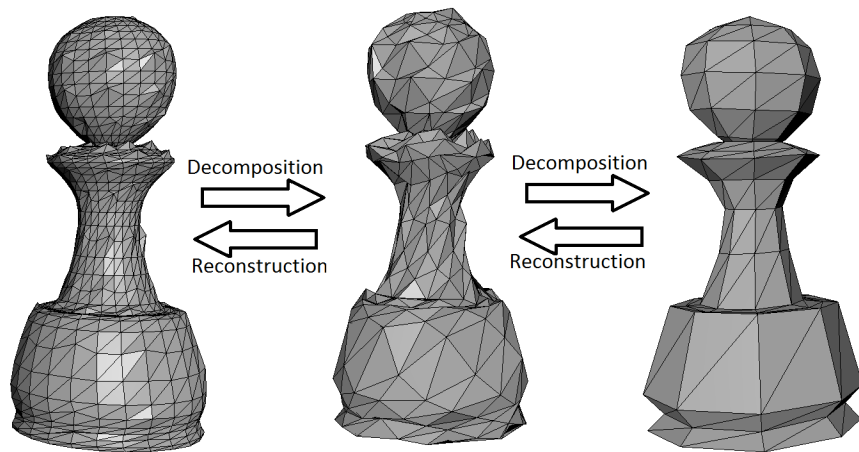

Figure 28: The act of decomposition and reconstruction on the pawn model that has been subdivided twice using $\sqrt{3}$ subdivision with vertices being randomly displaced.

The above examples testify that our proposed multiresolution framework enjoys stability when vertices are randomly and locally perturbed. However, similar to multiresolution techniques constructed by reversing a smooth subdivision, a local deviation from the original vertices may happen. Here, we quantify the amount of the local deviation of our multiresolution construction. Having the coefficients provided by equation (5.2) and (5.3), we can relate a coarse vertex $\bar{c}_k \in \bar{\mathbf{c}} = \mathbf{A}\mathbf{g}$, its correspondent high resolution vertex $g_k \in \mathbf{g}$, and its neighbors $g_{k+\lambda} \in \mathbf{g}$ as follows:

$$
\begin{aligned}
\bar{c}_k &= \frac{2}{2 - 3\alpha_{n_k}} g_k - \frac{\alpha_{n_k}}{n(2 - 3\alpha_{n_k})} \sum_{\lambda=1}^{n_k} g_{k+\lambda} \\
&= \frac{2}{2 - 3\alpha_{n_k}} g_k - \frac{3\alpha_{n_k}}{2 - 3\alpha_{n_k}} Ave \\
&= g_k + \frac{3\alpha_{n_k}}{2 - 3\alpha_{n_k}} (g_k - Ave) \\
&= g_k + \frac{3\alpha_{n_k}}{2 - 3\alpha_{n_k}} \ell \\
&= g_k + \beta\ell,
\end{aligned}
\tag{10.1}
$$

where $Ave = \frac{\sum_\lambda g_{k+\lambda}}{n}$ is the centroid of 1-ring neighborhood of g_k, $\ell = g_k - Ave$ is the Laplacian vector of g_k, connecting Ave to g_k, and $\beta = \frac{3\alpha_{n_k}}{2 - 3\alpha_{n_k}}$.

Equation (10.1) indicates that coarse vertices ($\bar{c}_k$) are determined by adding a vector along the Laplacian (ℓ) of the fine point (Figure 29). This vector is controlled by a scalar ($\beta = \frac{3\alpha_{n_k}}{2 - 3\alpha_{n_k}}$), which is dependent on α_{n_k}, and therefore the valence of vertex g_k. This scalar (β) is multiplied by the Laplacian (ℓ) to finally determine the location of the coarse vertex $\bar{c}_k$. Figure 29 illustrates ℓ, g_k, and $\bar{c}_k$, and it also shows how β changes for different valences.

Knowing the source of the local deviation, we can rearrange the multiresolution to obtain smoother meshes after decomposition. As explained by equation (10.1), the local deviation of vertex $\bar{c}_k$ is controlled by β which itself is defined based on α_{n_k}. By playing with the value of α_{n_k}, we can define smoother decompositions. For instance, when $\alpha_{n_k} < \frac{1}{3}$, only a fraction of ℓ is added to g_0 to compute $\bar{c}_0$. We should consider that when we change α_{n_k}, the values of matrices dependent on α_{n_k} (i.e., $\mathbf{P}, \mathbf{A}, \mathbf{B}, \mathbf{Q}$) change accordingly. However, the structures of matrices and the process of reconstruction remain the same and no information is lost after reconstruction. Figure 30 illustrates how we can control the local deviation of decomposition by changing the value of α_{n_k}.
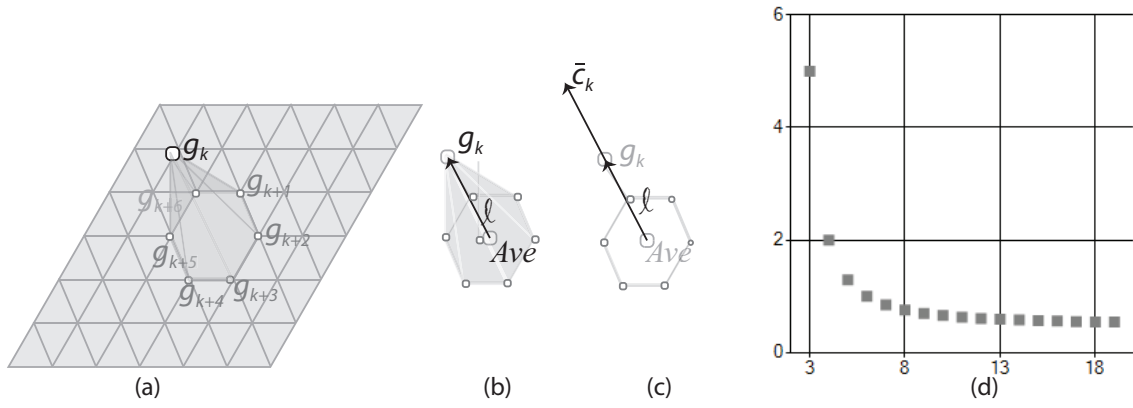
Figure 29: (a) Vertex g_k and its neighbors $g_{k+\lambda}$. (b) Ave is the centroid of $g_{k+\lambda}$ (neighbors of g_k), ℓ connects Ave to g_k. (c) $\bar{c}_k$ which is the decomposed vertex of g_0 is determined by adding $\beta\ell$ to g_k. Since g_k has six neighbors, β is one. (d) Relation between valence and β in the $\sqrt{3}$ subdivision; vertical axis is β and horizontal axis is valence.
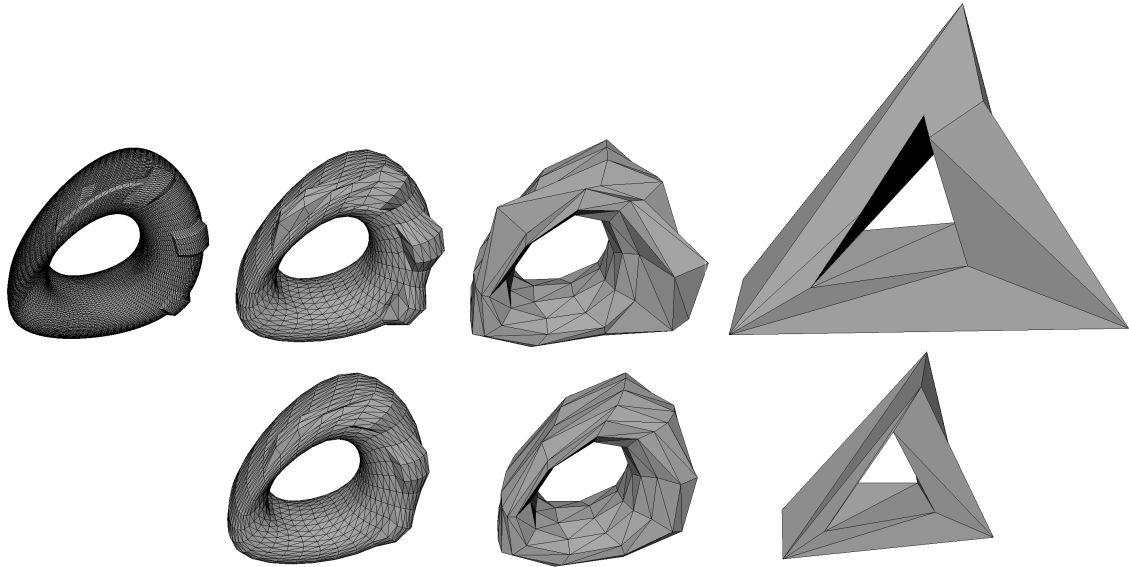

Figure 30: Comparison between decompositions with α_{n_k} of the $\sqrt{3}$ subdivision (top) and $\alpha_{n_k} = \frac{1}{8}$ (bottom). It is clear that when $\alpha_{n_k} = \frac{1}{8}$, local deviation is far less.
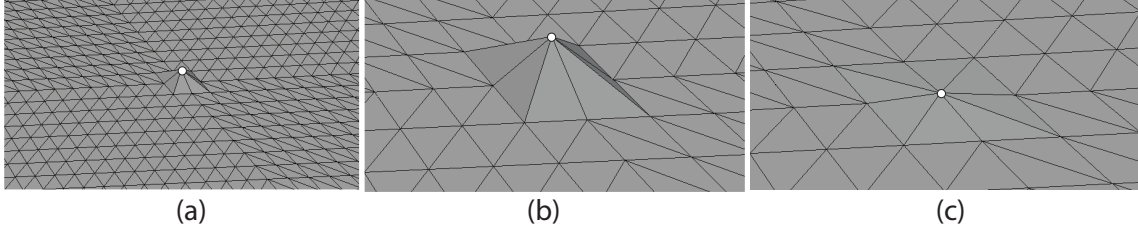
Figure 31: (a) Small perturbation on an irregular vertex with valence eight in top-left results in local deviation after decomposing the mesh (b). Adding δ can significantly reduce this local deviation (c). Only even resolutions are illustrated.

In addition to work with α_{n_k} to reduce the local deviation, it is possible to use a lifting scheme through a local optimization process to reduce the local deviation after decomposition [8]. To do so, coarse vertices $(\bar{c}_k)$ are added by a smoothing vector δ that is found based on the details in the neighborhood of $\bar{c}_k$. Note that δ is to reduce local errors in the neighborhood of $\bar{c}_k$. In fact, $\bar{c}_k$ is relaxed by δ, minimizing error (E_{Sub}) defined as in equation (10.2) below. We define E_{Sub} based on the 1-ring neighborhood of $\bar{c}_k$ in a $\sqrt{3}$ subdivision as

$$
\begin{aligned}
E_{Sub} &= \left\| g_k - (\tilde{g}_k + (1-\alpha_{n_k})\delta) \right\|^2 + \left\| g_{k+1} - (\tilde{g}_{k+1} + \frac{1}{3}\delta) \right\|^2 + ... + \left\| g_{k+n_k} - (\tilde{g}_{k+n_k} + \frac{1}{3}\delta) \right\|^2 \\
&= \left\| e_k - (1-\alpha_{n_k})\delta \right\|^2 + \left\| d_{k+1} - \frac{1}{3}\delta \right\|^2 + ... + \left\| d_{k+n_k} - \frac{1}{3}\delta \right\|^2,
\end{aligned}
$$

where the norm being used is the Euclidean norm. To find δ minimizing E_{Sub}, which is a quadratic function, its gradient is set to zero, $\nabla E_{sub} = 0$ and δ is obtained as:

$$
\delta = \frac{\frac{3\alpha_{n_k}}{2n}(1-\alpha_{n_k}) + \frac{1}{3}}{(1-\alpha_{n_k})^2 + \frac{n_k}{9}} \sum_{\lambda=1}^{n_k} d_{k+\lambda}.
$$

Having δ, we reduce the error of $\bar{c}_k$. Consequently, given a mesh with $\sqrt{3}$ subdivision connectivity, coarse vertices are initially determined using the matrix $\mathbf{A}$. These vertices are later smoothed by adding δ to each coarse vertex $\bar{c}_k$. To reconstruct g_k, δ is subtracted from $\bar{c}_k$, and the same reconstruction process is applied. Figure 31 illustrates that adding δ to a decomposed irregular vertex is very effective in reducing the local deviation of the decomposition process.

We can also formulate this process similar to the lifting scheme. This way, in fact, matrix $\mathbf{A}$ is modified to capture the effect of δ and can be defined as $\tilde{\mathbf{A}} = \mathbf{A} + \mathbf{LB}$, where the matrix $\mathbf{L}$ captures the coefficients of the $d_{k+\lambda}$ appearing in the δ equation. As a result of changing $\mathbf{A}$, the matrix

39

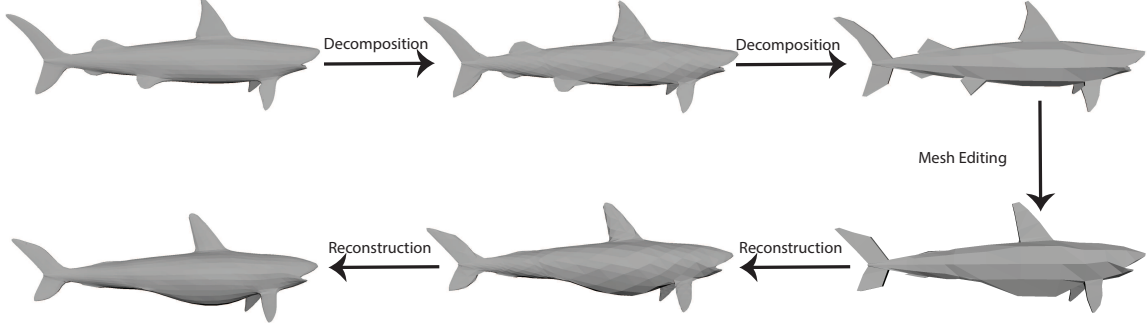Figure 32: Multiresolution construction with lifting.

Figure 33: Editing a high resolution mesh by decomposing it into a low resolution mesh and reconstructing the high resolution edited mesh.

$\mathbf{Q}$ is modified to $\tilde{\mathbf{Q}} = \mathbf{Q} - \mathbf{PL}$, to compensate adding δ vectors to coarse points. This process decomposes and reconstructs the mesh exactly the same as adding and subtracting δ from each coarse point. Figure 32 illustrates the whole process of lifting in the constraining wavelet approach when δ for each point is captured by the vector $\boldsymbol{\Delta}$.

One main application of reverse subdivision is mesh editing. Since a mesh with subdivision connectivity is usually composed of many vertices, editing such a mesh is usually a tedious task. As a result, it is useful to decrease the resolution of the mesh, edit it, and reconstruct the high resolution object. Figure 33 illustrates the application of our reverse subdivision for editing a mesh. To obtain these results, we used the ACM data structure [11, 33]. The advantage of this data structure is that details and coarse vertices can be easily distinguished from each other and are accessible through simple neighborhood vectors.

11. Conclusion and Future Work

We generalized diagrammatic approaches for subdivision of a general surface with a general connectivity that might have extraordinary points. In our proposed method, we represented the interactions by diagrams to obtain multiresolution masks. Some linear equations were derived from

the interactions of the diagrams satisfying the biorthogonality property of multiresolution. We examined our diagrammatic approach for the $\sqrt{3}$ subdivision in addition to the Catmull-Clark and Loop subdivisions.

There are many directions in which this work can be extended. Exploring the connection between our proposed approach and the Discrete Fourier Transform (DCT) is particularly interesting. Taking the same approach to find multiresolution for dual schemes such as the Doo Sabin is also of interest. Using the proposed multiresolution for a specific application such as compression, mesh editing, or data transmission may also be a rewarding research path.

Appendix A. Boundary Filters

Here, we provide filter values for the boundary. Based on our discussion in Section 9, the b values are:

$$
\begin{aligned}
b_1 &= -\frac{360908824401952}{6124761750733245} \\
b_2 &= \frac{821150352767744}{6124761750733245} \\
b_3 &= \frac{324486832948544}{6124761750733245} \\
b_4 &= -\frac{227763072235964}{680529083414805} \\
b_5 &= \frac{276752921024}{1311231374595} \\
b_6 &= \frac{34302231721304}{680529083414805} \\
b_7 &= -\frac{149920452798584}{6124761750733245} \\
b_8 &= -\frac{412135978326626}{6124761750733245} \\
b_9 &= \frac{276003571289944}{6124761750733245} \\
b_{10} &= -\frac{1740361028}{513090537885} \\
b_{11} &= -\frac{4404178928}{513090537885} \\
b_{12} &= \frac{1935707674}{513090537885}.
\end{aligned}
\tag{A.1}
$$

The q values are also listed as

$$
\begin{aligned}
q_1 &= \tfrac{11710197}{17758786} \\
q_2 &= \tfrac{13321692}{8879393} \\
q_3 &= 1 \\
q_4 &= \tfrac{11774114}{8879393} \\
q_5 &= -\tfrac{39839315}{17758786}.
\end{aligned}
\tag{A.2}
$$

[1] R. H. Bartels, F. F. Samavati, Multiresolutions numerically from subdivisions, Computers and Graphics 35 (2) (2011) 185–197.

[2] F. F. Samavati, R. H. Bartels, Diagrammatic tools for generating biorthogonal multiresolutions, International Journal of Shape Modeling 12 (1) (2006) 47–73.

[3] L. P. Kobbelt, $\sqrt{3}$ subdivision, in: SIGGRAPH'00: Proceedings of the 27th Annual Conference on Computer Graphics and Interactive Techniques, 2000.

[4] C. Loop, Smooth subdivision surfaces based on triangles, Master's thesis, Department of Mathematics, University of Utah (1987).

[5] E. Catmull, J. Clark, Recursively generated B-spline surfaces on arbitrary topological meshes, Comput. Aided Des. 10 (6) (1978) 350–355.

[6] E. J. Stollnitz, T. D. DeRose, D. H. Salesin, Wavelets for Computer Graphics, Morgan Kaufmann Publishers, 1996.

[7] G. Strang, T. Nguyen, Wavelets and Filter Banks, Wellesley-Cambridge Press, 1996.

[8] L. J. Olsen, F. F. Samavati, R. H. Bartels, Multiresolution for curves and surfaces based on constraining wavelets, Computers & Graphics 31 (3) (2007) 449 – 462.

[9] L. J. Olsen, F. F. Samavati, A discrete approach to multiresolution curves and surfaces, in: Proceedings of the 2008 International Conference on Computational Sciences and Its Applications, IEEE Computer Society, 2008, pp. 468–477.

[10] A. Mahdavi-Amiri, F. F. Samavati, ACM: Atlas of connectivity maps for semiregular models, in: Proceedings of Graphics Interface 2013, GI '13, 2013, pp. 99–107.

[11] A. Mahdavi-Amiri, F. F. Samavati, Atlas of connectivity maps, Computers & Graphics 39 (0) (2014) 1 – 11.

[12] F. F. Samavati, N. Mahdavi-Amiri, R. H. Bartels, Multiresolution surfaces having arbitrary topologies by a reverse Doo-Sabin subdivision method, Computer Graphics Forum 21 (2) (2002) 121–136.

[13] R. H. Bartels, F. F. Samavati, Reversing subdivision rules: Local linear conditions and observations on inner products, Journal of Computational and Applied Mathematics 119 (1–2) (2000) 29–67.

[14] M. Bertram, Biorthogonal Loop-Subdivision Wavelets, Computing 72 (1-2) (2004) 29–39.

[15] F. Payan, C. Roudet, B. Sauvage, Semi-regular triangle remeshing: A comprehensive study, Computer Graphics Forum 34 (1) (2015) 86–102.

[16] D. Bommes, B. Levy, N. Pietroni, E. Puppo, C. S. a, M. Tarini, D. Zorin, State of the art in quad meshing, in: Eurographics STARS, Vol. 31, 2012, pp. 1–24.

[17] P. Alliez, G. Ucelli, C. Gotsman, M. Attene, Recent advances in remeshing of surfaces, State-of-the-art report, AIM@SHAPE EU Network (2005).

[18] E. J. Stollnitz, T. D. Derose, D. H. Salesin, Wavelets for Computer Graphics: Theory and Applications, Morgan Kaufmann Publishers Inc., 1996.

[19] A. W. F. Lee, D. Dobkin, W. Sweldens, P. Schröder, Multiresolution mesh morphing, in: Proceedings of the 26th annual conference on Computer graphics and interactive techniques, SIGGRAPH '99, ACM Press/Addison-Wesley Publishing Co., New York, NY, USA, 1999, pp. 343–350.

[20] H. Hoppe, E. Praun, Shape compression using spherical geometry images, in: N. Dodgson, M. Floater, M. Sabin (Eds.), Advances in Multiresolution for Geometric Modelling, Mathematics and Visualization, Springer Berlin Heidelberg, 2005, pp. 27–46.

[21] H. Hoppe, View-dependent refinement of progressive meshes, in: Proceedings of the 24th Annual Conference on Computer Graphics and Interactive Techniques, SIGGRAPH '97, 1997, pp. 189–198.

[22] M. Eck, T. DeRose, T. Duchamp, H. Hoppe, M. Lounsbery, W. Stuetzle, Multiresolution analysis of arbitrary meshes, in: Proceedings of the 22nd annual conference on Computer graphics and interactive techniques, SIGGRAPH '95, ACM, 1995, pp. 173–182.

[23] G. Taubin, Geometric Signal Processing on Polygonal Meshes, in: Eurographics 2000 - STARs, Vol. 4, Eurographics Association, 2000, pp. 81–96. `doi:10.2312/egst.20001029`.

[24] H. Zhang, O. Van Kaick, R. Dyer, Spectral mesh processing, in: Computer graphics forum, Vol. 29, Wiley Online Library, 2010, pp. 1865–1894.

[25] L. J. Olsen, Constraining wavelets for multiresolution, Master's thesis, University of Calgary (2006).

[26] A. Finkelstein, D. H. Salesin, Multiresolution curves, in: A. Glassner (Ed.), Proceedings of SIGGRAPH '94 (Orlando, Florida, July 24–29, 1994), Computer Graphics Proceedings, Annual Conference Series, ACM SIGGRAPH, ACM Press, 1994, pp. 261–268.

[27] W. Sweldens, The lifting scheme: A construction of second generation wavelets, SIAM Journal on Mathematical Analysis 29 (2) (1998) 511–546.

[28] J. Sadeghi, F. F. Samavati, Smooth reverse subdivision, Computers & Graphics 33 (3) (2009) 217 – 225, International Conference on Shape Modelling and Applications 2009.

[29] J. Sadeghi, F. F. Samavati, Smooth reverse Loop and Catmull-Clark subdivision, Graphical Models 73 (5) (2011) 202–217.

[30] F. F. Samavati, R. H. Bartels, Multiresolution curve and surface representation by reversing subdivision rules, Computer Graphics Forum 18 (2) (1999) 97–119.

[31] J. Goswami, A. Chan, Fundamentals of Wavelets: Theory, Algorithms, and Applications, Wiley Series in Microwave and Optical Engineering, Wiley, 2011.

[32] S. Lanquetin, M. Neveu, Reverse catmull-clark subdivision, in: WSCG 2006: Full Papers Proceedings: The 14-th international Conference in Central Europe on Computer Graphics, Visualization and Computer Vision 2006: University of West Bohemia, Plzen, Czech Republic, January 31 February 2, Václav Skala-UNION Agency, 2006, pp. 319–326.

[33] A. Mahdavi-Amiri, F. Samavati, Connectivity maps for subdivision surfaces, in: GRAPP/IVAPP, 2012, pp. 26–37.

590